IEEE Access
Multidisciplinary | Rapid Review | Open Access Journal

Date of publication xxxx 00, 0000, date of current version xxxx 00, 0000.

*Digital Object Identifier 10.1109/ACCESS.2020.Doi Number*

# A Model-based Tightly Coupled Architecture for Low-Cost Unmanned Aerial Vehicles for Real-Time Applications

**Hery A. Mwenegoha[1], Terry Moore[1], James Pinchin[1], and Mark Jabbal[2]**

[1] Nottingham Geospatial Institute, University of Nottingham, Triumph Road, Nottingham NG7 2TU, UK
[2] Fluids and Thermal Engineering Research Group, University of Nottingham, Nottingham NG7 2RD, UK

Corresponding author: Hery A. Mwenegoha (e-mail: hery.mwenegoha1@nottingham.ac.uk)

The work is funded by the INNOVATIVE doctoral programme. The INNOVATIVE programme is partially funded by the Marie Curie Initial Training Networks (ITN) action (project number 665468) and partially by the Institute for Aerospace Technology (IAT) at the University of Nottingham.

**ABSTRACT** This paper investigates the navigation performance of a vehicle dynamic model-based (VDM-based) tightly coupled architecture for a fixed-wing Unmanned Aerial Vehicle (UAV) during a global navigation satellite system (GNSS) outage for real-time applications. Unlike an Inertial Navigation System (INS) which uses inertial sensor measurements to propagate the navigation solution, the VDM uses control inputs from either the autopilot system or direct pilot commands to propagate the navigation states. The proposed architecture is tested using both raw GNSS observables (Pseudorange and Doppler frequency) and Micro-Electro-Mechanical Systems-grade (MEMS) Inertial Measurement Unit (IMU) measurements fused using an extended Kalman filter (EKF) to aid the navigation solution. Other than the navigation states, the state vector also includes IMU errors, wind velocity, VDM parameters, and receiver clock bias and drift. Simulation results revealed significant performance improvements with a decreasing number of satellites in view during 140 seconds of a GNSS outage. With two satellites visible during the GNSS outage, the position error improved by one order of magnitude as opposed to a tightly coupled INS/GNSS scheme. Real flight tests on a small fixed-wing UAV show the benefits of the approach with position error being an order of magnitude better as opposed to a tightly coupled INS/GNSS scheme with two satellites in view during 100 seconds of a GNSS outage.

**INDEX TERMS** Aircraft navigation, GNSS outage, Inertial navigation, Model-based navigation, Tightly coupled, TCVDM, Unmanned aerial vehicles, Vehicle dynamic model, VDM

## I. INTRODUCTION

Low-cost (sub $12,000), low-mass (sub 20 kg) Unmanned Aerial Vehicles (UAVs) have found significant applications in Dull, Dangerous and Dirty "D-D-D" fields. UAVs are used in aerial mapping, search and rescue, resource management and conservation efforts, and delivery of medical products, to name a few [1], [2].

A navigation system is an integral part of a UAV, its estimation of position, velocity, and attitude can be used by the payload as well as being used in guidance and control of the aircraft. UAVs commonly use an inertial navigation system (INS) integrated with a global navigation satellite system (GNSS) to provide a filtered and quasi-continuous navigation solution. Rapid dynamics, severe multipath, and interference can cause a GNSS outage during which the navigation solution will degrade [3]–[6]. In reducing the drift of the navigation solution, some authors have explored advanced error modelling schemes which avoid adding weight but introduce additional software complexities [6], [7]. Others have explored advanced integration schemes such a tight and ultra-tight coupling, but the navigation solution is still INS-based, which can be disabled in case of inertial measurement unit (IMU) failure [4], [8].

More recently, some authors have explored the use of a vehicle dynamic model (VDM) as either the main process model in a model-based approach [9]–[11] or as an aiding tool in a model-aided approach [12]–[14]. The use of a VDM has gained popularity amongst researchers because it can significantly improve navigation performance without adding extra weight to the overall system and can meet the stringent cost and power requirements, inherent in low-cost UAV applications [11].

Sendobry [9] used a quadrotor dynamic model to propagate navigation states whilst other sensors provided

corrections to the navigation solution. The approach avoids duplicate states and showed significant performance improvements, even in the presence of VDM parameter errors. Khaghani and Skaloud [10], and Mwenegoha *et al.* [11] extended the model-based approach proposed by Sendobry to fixed-wing UAVs. Simulation results revealed two orders of magnitude improvement in position estimation during extended GNSS outages. However, the navigation performance with decreasing number of satellites in view was not investigated because the proposed schemes relied on filtered GNSS measurements (position, velocity) which are not available during an outage.

Koifman and Bar-Itzhack [12] proposed a multi-process model approach that combined a VDM and an INS in a fusion filter with the final solution being derived from the INS. Even though the approach introduced duplicate states, the authors showed that the position error of the aided INS was relatively low as opposed to the unaided case. Also, they showed that the inclusion of the VDM parameters and wind in the state vector improved the stability of the filter and reduced error growth, especially in the presence of VDM parameter errors and wind. Zahran *et al.* [13] derived a VDM from a hybrid machine learning scheme utilising a bagged regression and classification technique to aid an INS during a GNSS outage. The approach showed significant improvements in position estimation during an outage. However, compound manoeuvres not included in the training data seemed to degrade the performance during a GNSS outage. Further, the performance of the algorithm was investigated through simulations for a quadcopter UAV and the mechanism for direct wind estimation was not included. Youn *et al.* [14] proposed a model-aided state estimation for a fixed-wing UAV with synthetic measurements. Even though the approach included a mechanism for direct wind estimation, the uncertainty of VDM parameters on navigation performance was not considered. Further, the impact of a GNSS outage on navigation performance was not investigated. Mueller *et al.* [15] used a unified model-aided technique with a MEMS-grade IMU in a quadrotor and demonstrated significant position error reduction during a GNSS outage. The state vector was augmented to include drag coefficient terms and wind velocity. It was shown that the inflight estimation of wind velocity significantly improved the estimation of IMU error terms and drag coefficient terms. Further, it was shown that the quality of the IMU plays an important role in wind velocity estimation during a GNSS outage with a higher grade IMU showing improved wind estimation. However, the approach only considered the translational dynamic model and ignored the rotational model. Further, the approach relied on filtered GNSS measurements which are not available when tracking less than four satellites.

The vast majority of VDM integration schemes in the literature rely on using filtered GNSS measurements output by a GNSS receiver to provide a bounded navigation solution. These measurements are usually not available during a GNSS outage or when tracking less than four satellites, which can cause the navigation solution to drift even when using a VDM [9]–[11], [13], [16]. Further, model-aided INS schemes can easily be disabled in case of IMU failure and additionally, multi-process model schemes introduce duplicate states that increase computational cost [17].

Therefore, we present an innovative tightly coupled vehicle dynamic model-based architecture (TCVDM) that is capable of taking full advantage of available raw observables from a GNSS receiver even when tracking one satellite as shown in Fig. 1. A specific case to a fixed-wing UAV is investigated which, alongside the raw observables, uses measurements from a low-cost MEMS-grade IMU to aid the navigation solution.

The proposed architecture is investigated using a Monte Carlo simulation study to test its navigation performance relative to a tightly coupled INS/GNSS integration architecture during a GNSS outage. Further, real flight tests are carried out on a small fixed-wing UAV fitted with low-cost GNSS receivers and a MEMS-grade IMU to assess its performance under operational conditions.

In this paper, several limitations of the TCVDM scheme vis-à-vis a tightly coupled INS/GNSS approach are addressed, most notably is that the architecture structure is dependent on the host platform type (quadrotor, fixed-wing, etc.). In this sense, we make the following contributions:

- A tightly coupled model-based integration architecture that significantly mitigates drift in the navigation solution during a GNSS outage is proposed.
- Monte Carlo simulation results of the proposed architecture are presented and analysed, along with comparisons to a standard tightly coupled INS/GNSS approach.
- A GNSS measurement simulator used to derive raw GNSS observables used in the fusion filter is presented.
- Navigation performance results of the proposed approach using real flight data from a small UAV are presented and analysed.

In the next section the proposed TCVDM architecture is presented. In Section III, the simulation setup used to examine the proposed approach is presented. Simulation results are presented in Section IV, and the experimental setup alongside real flight test results are presented in Section V. Conclusions are drawn in Section VI.

## II. PROPOSED CONCEPT

### A. TCVDM ARCHITECTURE

The architecture (Fig. 1) uses control inputs ($U$) to drive the navigation solution. The state vector is augmented to include IMU error terms, wind velocity components, VDM parameters and the receiver clock bias and drift terms. The proposed architecture significantly mitigates drift of the

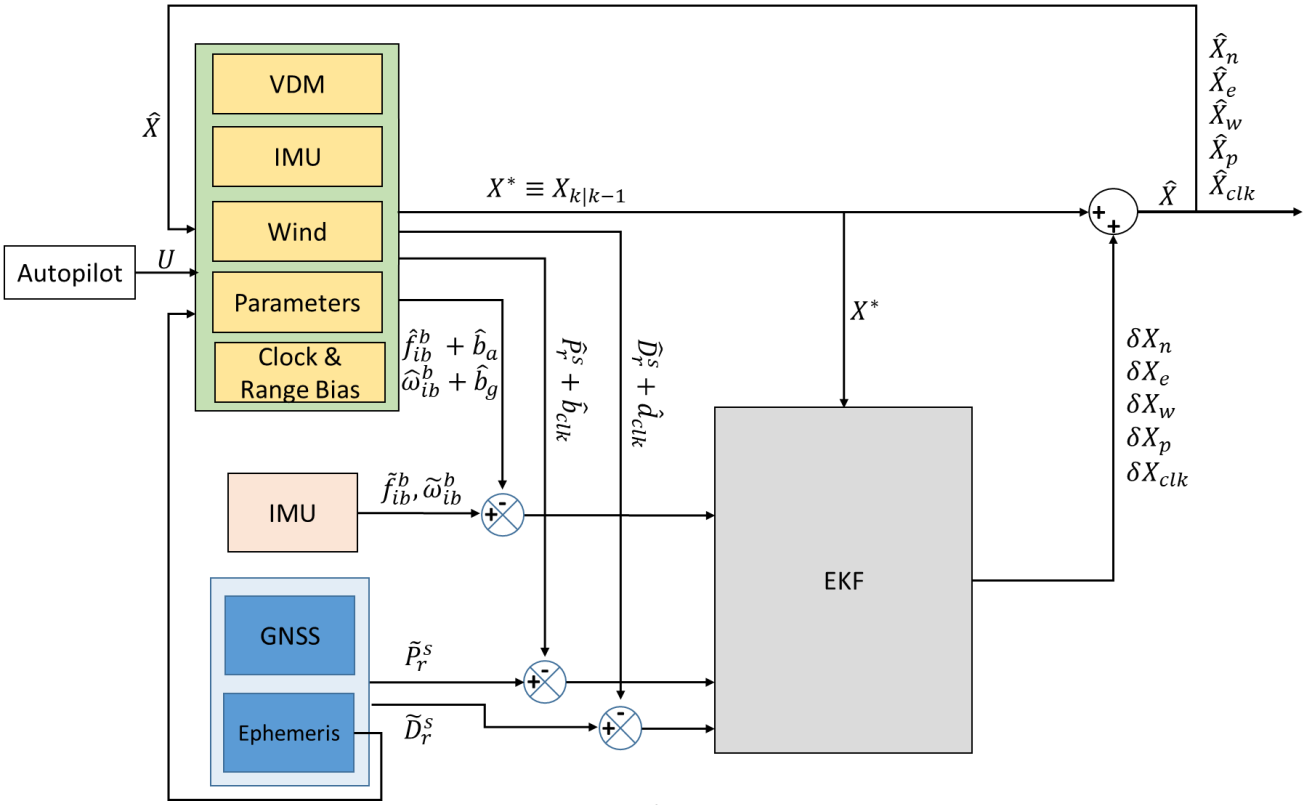


**FIGURE 1.** **TCVDM architecture. $X^*$ represents the predicted state vector, $\hat{X}$ is the updated state vector which includes the navigation states $X_n$, IMU error terms $X_e$, wind velocity components $X_w$, VDM parameters $X_p$ and receiver clock terms $X_{clk}$, respectively. $\hat{P}_r^s$ and $\tilde{P}_r^s$ represent the predicted and measured pseudorange; $\hat{D}_r^s$ and $\tilde{D}_r^s$ represent the predicted and measured Doppler frequency. $f_{ib}^b, \omega_{ib}^b$ represent the specific force and angular rate, respectively. $U$ is the control input vector for aileron $\delta_a$, elevator $\delta_e$, and rudder $\delta_r$ deflection as well as commanded propeller speed $n_c$.**

navigation solution during a GNSS outage validated via a Monte Carlo simulation study.

Control inputs, which include the control surface deflections and the commanded propeller speed, are used to propagate the navigation states using the rigid body equations of motion for a fixed-wing UAV. An additional input to the VDM is wind velocity vector. Most fixed-wing UAVs are equipped with an air data system, but the proposed architecture makes it possible to estimate wind velocity components within the navigation filter itself. Since the VDM is used as the main process model no additional sensors, other than an IMU and a GNSS receiver, are required. An IMU, unlike a VDM, is usually affected by platform vibrations and thermal effects. On the other hand, GNSS signals can experience severe multipath or a receiver can be affected by platform dynamics leading to a GNSS outage. The use of a VDM as the main process model ensures a continuous navigation solution regardless of the underlying conditions unless there is a hardware failure of the navigation system. The state vector is augmented to include IMU errors and GNSS receiver clock errors so that these errors can be estimated and removed from the measurements output by the IMU and GNSS receiver. A VDM requires careful consideration of its structure because it depends on the host platform type. Therefore, having an accurate model or a set of model parameters is essential for successful VDM-based navigation. These parameters can be determined through laborious calibration routines or system identification techniques. However, our approach is similar to the one proposed by Khaghani and Skaloud [10] in that the state vector includes the model parameters, enabling their estimation during a flight. This significantly reduces the effort required in system identification and allows for some variation of the model parameters. This is essential because it would allow changing some aspects of the aircraft such as the payload or the propeller without a new system identification routine. The capability for online parameter calibration is discussed briefly in Section IV and the interested reader is directed to [11] for an in-depth analysis for a loosely coupled scheme. It is important to note that we do not aim to present a complete solution to the parameter estimation problem but rather show the navigation performance achieved with some parameter uncertainty.

In the augmented state vector, IMU error terms, wind velocity components and the VDM parameters are propagated using a random walk process. A second-order Gauss-Markov process is used to model the receiver clock bias and drift.

An EKF is used to estimate corrections to the navigation states using measurements from an IMU and a GNSS receiver. The novel part of the proposed architecture is in the use of raw GNSS observables alongside IMU measurements with a VDM-based navigation scheme.

### B. COORDINATE FRAMES

Fig. 2 shows the main coordinate frames used in the research.

An Inertial frame (not shown in Fig. 2) is a non-rotating, non-accelerating frame with respect to the rest of the universe. This definition results in a non-unique reference frame. Here, an Earth-centred frame approximates the inertial frame with its x-axis pointing from the Earth to the Sun at the vernal equinox. The celestial pole defines the z-axis and the y-axis completes the 3D right-handed Cartesian system.

A local navigation frame (North, East, Down) has the same origin as a body-fixed frame and is used as the resolving frame for the navigation solution. Its z-axis ($Z_D$) is defined as the normal to the surface of the reference ellipsoid and points to the local nadir. Its x-axis ($X_N$) points to north and by completing the orthogonal set the y-axis ($Y_E$) points to east.

A body-fixed frame as the name suggests has its axes fixed with respect to the body. The convention used in our research is such that the x-axis ($X_b$) points in the forward direction, the z-axis ($Z_b$) points down and the y-axis ($Y_b$) completes the orthogonal set. IMU measurements are usually made in the body-fixed frame and hence $X_b, Y_b$ and $Z_b$ are sometimes known as roll, pitch and yaw axes.

Aerodynamic forces are defined in the wind frame with its x-axis pointing in the direction of the airspeed ($V$). A transformation matrix $R_w^b$ is used to transform the aerodynamic forces in the wind frame to the body frame.

An Earth-centred Earth-fixed frame (ECEF) defines the reference frame used in the formulation. The ECEF frame (not shown in Fig. 2) has its origin at the centre of the ellipsoid modelling the Earth's surface and remains fixed with respect to the Earth. This is an equatorial frame with its x-axis pointing to the intersection of the equator with the conventional zero meridian. The z-axis points along the Earth's axis of rotation and the y-axis completes the orthogonal set.

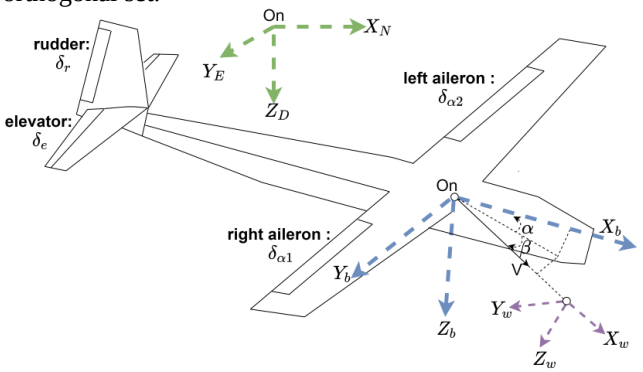


**FIGURE 2. Body (b), navigation (n), and wind (w) coordinate frames and the control surfaces on the aircraft. $V$ is the airspeed, $\alpha$ and $\beta$ are angle of attack and sideslip angle, respectively. $\delta_{[a,e,r]}$ are control deflections.**

Formulation details of the angle of attack, sideslip angle, dynamic pressure, as well as the atmospheric model used are provided in Table I.

TABLE I.
AIRSPEED, ANGLE OF ATTACK, SIDESLIP ANGLE AND ATMOSPHERIC MODEL

| **Airspeed ($V$), $\alpha$, $\beta$** | **Atmosphere** |
|---|---|
| $v^b = V^b + R_n^b W^n$ | $T = T_0\left[1 + a\frac{h_{amsl}}{T_0}\right]$ |
| $V^b = \left[V_x^b\ V_y^b\ V_z^b\right]^T$ | $h_{amsl} \approx h - N(\mu, \lambda)$ |
| $V = \|V^b\|$ | $\rho = \frac{p_0\left[1 + a\frac{h_{amsl}}{T_0}\right]^{5.2561}}{R\,T}$ |
| $\alpha = \arctan\left(\frac{V_z^b}{V_x^b}\right)$ | $\bar{q} = 1/2\rho(V^b)^2$ |
| $\beta = \arcsin\left(\frac{V_y^b}{V}\right)$ | |
| where: | where: |
| $R_n^b$ : NED to body frame rotation matrix | $\rho$ : air density |
| $W^n$: wind vector in the NED frame | $R$ : specific gas constant |
| | $T_0$ : sea-level temperature |
| | $N(\mu, \lambda)$: Geoid height |
| | $h$ : Geodetic height |

### C. EQUATIONS OF MOTION

The TCVDM navigation states considered in the simulation are presented below:

$$X_n = \left[r_{eb}^n\ v_{eb}^n\ q_b^n\ \omega_{ib}^b\ n\right]^T \tag{1}$$

where $r_{eb}^n = [\mu\ \lambda\ h]^T$, is the geodetic position vector representing latitude, longitude and height respectively, $v_{eb}^n = \left[v_{eb,N}^n\ v_{eb,E}^n\ v_{eb,D}^n\right]^T$, is the velocity vector in the NED coordinate frame. $q_b^n = [q_0\ q_1\ q_2\ q_3]^T$ is the quaternion vector representing rotation from the body frame to the NED coordinate frame, $\omega_{ib}^b$ is the rotation rate vector around the body axes with respect to an inertial frame and $n$ is the propeller speed.

$$\dot{r}_{eb}^n = \left[\frac{v_{eb,N}^n}{R_M + h}, \frac{v_{eb,E}^n}{(R_P + h)\,cos(\mu)}, -v_{eb,D}^n\right]^T \tag{2}$$

$$\dot{v}_{eb}^n = R_b^n f_{ib}^b + g^n - (2\Omega_{ie}^n + \Omega_{en}^n)v_{eb}^n \tag{3}$$

$$\dot{q}_b^n = \frac{1}{2} q_b^n \otimes \left[\omega_{nb}^b\right] = \frac{1}{2}\left[\omega_{nb}^b\right]_R q_b^n \tag{4}$$

$$\dot{\omega}_{ib}^b = (I^b)^{-1}(M - \omega_{ib}^b \times I^b \omega_{ib}^b) \tag{5}$$

$$\dot{n} = \frac{n_c}{\tau_n} - \frac{n}{\tau_n} \tag{6}$$

In (2)-(6) above, $R_M$ and $R_P$ represent the meridian radius of curvature and prime vertical radius of curvature, respectively, $f_{ib}^b$ is the specific force vector with respect to an inertial frame, $g^n$ is the gravity vector in the NED frame. $M$ is the moment vector, $I^b$ is the body inertia matrix with the components: $I_{xx}, I_{yy}, I_{zz}, I_{xz}$ representing the inertia terms about the respective axes. $n_c$ and $\tau_n$ represent the commanded propeller speed and time constant, respectively. The symbol $\otimes$ represents a quaternion product and $[\omega]_R$ represents the right-quaternion-product matrix for the vector $\omega = [\omega_1\ \omega_2\ \omega_3]^T$ given by:

$$[\omega]_R = \begin{bmatrix} 0 & -\omega_1 & -\omega_2 & -\omega_3 \\ \omega_1 & 0 & \omega_3 & -\omega_2 \\ \omega_2 & -\omega_3 & 0 & \omega_1 \\ \omega_3 & \omega_2 & -\omega_1 & 0 \end{bmatrix} \quad (7)$$

The rotation matrix $R_b^n$, is expressed in terms of the quaternion as:

$$R_b^n = \begin{bmatrix} q_0^2+q_1^2-q_2^2-q_3^2 & 2(q_1q_2-q_0q_3) & 2(q_1q_3+q_0q_2) \\ 2(q_0q_3+q_1q_2) & q_0^2-q_1^2+q_2^2-q_3^2 & 2(q_2q_3-q_0q_1) \\ 2(q_1q_3-q_0q_2) & 2(q_2q_3+q_0q_1) & q_0^2-q_1^2-q_2^2+q_3^2 \end{bmatrix} \quad (8)$$

In (4), $\omega_{nb}^b$ is given by:

$$\omega_{nb}^b = \omega_{ib}^b - (R_b^n)^T(\omega_{ie}^n + \omega_{en}^n) \quad (9)$$

where $\omega_{ib}^b$ is the body angular rate vector with respect to an inertial frame, $\omega_{en}^n$ is the transport-rate term and $\omega_{ie}^n$ is the earth rotation vector in the NED frame.

A skew-symmetric matrix $\Omega_{ab}^\gamma$ for a vector $\omega_{ab}^\gamma = [\omega_{ab_1}^\gamma \ \omega_{ab_2}^\gamma \ \omega_{ab_3}^\gamma]^T$ is defined as:

$$\Omega_{ab}^\gamma = \begin{bmatrix} 0 & -\omega_{ab_3}^\gamma & \omega_{ab_2}^\gamma \\ \omega_{ab_3}^\gamma & 0 & -\omega_{ab_1}^\gamma \\ -\omega_{ab_2}^\gamma & \omega_{ab_1}^\gamma & 0 \end{bmatrix} \quad (10)$$

and the product between a skew-symmetric matrix and a vector $v_c$ is given by:

$$\Omega_{ab}^\gamma \, v_c = \omega_{ab}^\gamma \times v_c, \quad \forall \, v_c \in \mathbb{R}^3 \quad (11)$$

The specific force term is represented by:

$$f_{ib}^b = \frac{1}{m}\left( R_w^b \begin{bmatrix} F_X^w \\ F_Y^w \\ F_Z^w \end{bmatrix} + \begin{bmatrix} F_T \\ 0 \\ 0 \end{bmatrix} \right) \quad (12)$$

$$R_w^b = \begin{bmatrix} \cos\alpha\cos\beta & -\cos\alpha\sin\beta & -\sin\alpha \\ \sin\beta & \cos\beta & 0 \\ \cos\beta\sin\alpha & -\sin\alpha\sin\beta & \cos\alpha \end{bmatrix}$$

$$F_X^w = \bar{q}S(CF_{X1} + CF_{X_\alpha}\,\alpha + CF_{X_{\alpha^2}}\,\alpha^2 + CF_{X_{\beta^2}}\,\beta^2) \quad (13)$$

$$F_Y^w = \bar{q}SCF_{Y1}\beta \quad (14)$$

$$F_Z^w = \bar{q}S\left(CF_{Z1} + CF_{Z_\alpha}\alpha\right) \quad (15)$$

$$F_T = \rho n^2 D^4\left(CF_{T_1} + CF_{T_2}J + CF_{T_3}J^2\right) \quad (16)$$

$$J = \frac{V}{D\pi n}$$

Moreover, the moment term is represented by:

$$M = [M_X^b \ M_Y^b \ M_Z^b]^T \quad (17)$$

$$M_X^b = \bar{q}Sb(CM_{X_{\delta_\alpha}}\delta_\alpha + CM_{X_{\bar{\omega}_x}}\bar{\omega}_x + CM_{X_{\bar{\omega}_z}}\bar{\omega}_z + CM_{X_\beta}\beta) \quad (18)$$

$$M_Y^b = \bar{q}S\bar{c}(CM_{Y_{\delta_e}}\delta_e + CM_{Y_{\bar{\omega}_y}}\bar{\omega}_y + CM_{Y_\alpha}\,\alpha + CM_{Y1}) \quad (19)$$

$$M_Z^b = \bar{q}Sb(CM_{Z_{\delta_r}}\delta_r + CM_{Z_{\bar{\omega}_z}}\bar{\omega}_z + CM_{Z_\beta}\,\beta) \quad (20)$$

$$\bar{\omega}_x = \frac{\omega_x b}{2V}, \bar{\omega}_y = \frac{\omega_y \bar{c}}{2V}, \bar{\omega}_z = \frac{\omega_z b}{2V} \quad (21)$$

$S$ is the wing area, $\bar{c}$ is the wing chord, $b$ the wingspan, $CM_{[X\,Y\,Z]_j}$ are the moment derivatives, $CF_{[X\,Y\,Z]_j}$ are the aerodynamic force derivatives and $CF_{T_{i=[1\,2\,3]}}$ are the thrust derivatives.

### D. FILTERING METHODOLOGY

An Extended Kalman Filter (EKF) [18], [19] is used in the estimation of corrections to the states ($\delta X$) using raw GNSS observables and IMU measurements. A linearized version of the process model ($F = \partial\dot{X}/\partial X$) and observation model ($H = \partial Z/\partial X$) are used in the EKF during the prediction and correction steps.

The navigation states ($X_n$) are propagated using (2)-(6).

IMU errors ($X_e$) are modelled using a random walk process in the filter given by:

$$\dot{X}_e = G_e\,u_e \quad (22)$$
$$X_e = [b_{ax}\ b_{ay}\ b_{az}\ b_{gx}\ b_{gy}\ b_{gz}]^T$$

where $G_e$ is the noise shaping matrix and $u_e$ is the noise vector. In (22), $b_{a|g\,[x\,y\,z]}$ represents the accelerometer and gyroscope bias, respectively. A random constant model is superposed in the random walk model by setting the initial uncertainty to match the standard deviation of the turn-on bias for the inertial sensors. In the simulator, a first-order Gauss-Markov process is used to model the inertial sensors.

Wind velocity ($X_w$) also follows a random walk process model in the filter given by:

$$\dot{X}_w = G_w\,u_w \quad (23)$$
$$X_w = [w_N\ w_E\ w_D]^T$$

In (23), $G_w$ is the noise shaping matrix for the wind velocity vector and $u_w$ is the driving noise vector. This model has been found to work well in the estimation of 3D wind after appropriate filter tuning. In the simulator, wind is modelled using a first-order Gauss-Markov process with a constant magnitude of 4 m/s and a process uncertainty of 0.1 m/s.

VDM parameter errors $X_p$ are propagated using a random walk process with small input noise components to improve the filter's stability. The VDM parameter vector, $X_p$, is presented below:

$$X_p = \begin{bmatrix} CF_{T_1},\ CF_{T_2},\ CF_{T_3},\ CF_{X_1},\ CF_{X_\alpha},\ CF_{X_{\alpha 2}}, \ldots \\ \ldots CF_{X_{\beta 2}},\ CF_{Z_1},\ CF_{Z_\alpha},\ CF_{Y_1},\ CM_{X_{\delta\alpha}},\ CM_{X_\beta}, \ldots \\ \ldots CM_{X_{\bar{\omega}_x}}, CM_{X_{\bar{\omega}_z}},\ CM_{Y_1},\ CM_{Y_\alpha}, CM_{Y_{\delta_e}}, CM_{Y_{\bar{\omega}_y}}, \ldots \\ \ldots CM_{Z_{\delta_r}},\ CM_{Z_{\bar{\omega}_z}}, CM_{Z_\beta},\ \tau_n \end{bmatrix}^T \quad (24)$$

In the simulator, the VDM parameters are treated as constant ($\dot{X}_p = 0$).

A second-order Gauss-Markov process is used to model the receiver clock ($X_{clk} = [b_{clk}\ \ d_{clk}]^T$) in both the filter and the simulator even though values used in each case are different. The receiver clock bias ($b_{clk}$) and drift ($d_{clk}$) dynamics are given by:

$$\dot{b}_{clk} = d_{clk} + u_f \quad (25)$$
$$\dot{d}_{clk} = u_g$$

In (25), $u_f$ and $u_g$ are independent white noise inputs to the clock model.

In the filter, the rotation vector error $\delta\psi$ is considered instead of the quaternion to simplify the assignment of uncertainties and the analysis altogether. Therefore, the quaternion error dynamics are approximated using the global rotation vector error. The perturbed quaternion is given by:

$$q_t = \delta q \otimes q \tag{26}$$

The global quaternion error dynamics is given by:

$$\delta\dot{q} = \begin{bmatrix} 0 \\ \frac{1}{2}\delta\psi \end{bmatrix} \tag{27}$$
$$\delta q \in \mathbb{R}^4 \text{ and } \delta\psi \in \mathbb{R}^3$$

Therefore, the state vector considered in the filter is given by:

$$x = \begin{bmatrix} r_{eb}^n & v_{eb}^n & \delta\psi^n & \omega_{ib}^b & n & X_e & X_w & X_p & X_{clk} \end{bmatrix}^T \tag{28}$$
and the dynamics:
$$\dot{x} = \begin{bmatrix} \dot{r}_{eb}^n & \dot{v}_{eb}^n & \delta\dot{\psi}^n & \dot{\omega}_{ib}^b & \dot{n} & \dot{X}_e & \dot{X}_w & \dot{X}_p & \dot{X}_{clk} \end{bmatrix}^T$$

The measurement vector ($Z_k$) consists of IMU measurements ($\tilde{f}_{ib}^b, \tilde{\omega}_{ib}^b$) and raw GNSS observables ($\tilde{P}_r^s, \tilde{D}_r^s$). Here, the measurements are represented using a measurement function ($h_m$) such that:

$$Z_k = h_m[x_k, u_k] + w_k \tag{29}$$

where $x_k$ is the predicted state vector at the current time index '$k$', $u_k$ is the control input vector and $w_k$ is the residual error for each measurement modelled as Gaussian white noise. Defining $E[\bullet]$ as the expectation operator, the measurement covariance $R_k$ is given by:

$$R_k = E[w_k\, w_k^T]$$
independent noise components dictate (30)
$$E[p_{ij}] = 0 \text{ for } i \neq j$$

Therefore, the observation model for the IMU is given by:

$$Z_{IMU} = \begin{bmatrix} f_{ib}^b + X_e([1\ 2\ 3]) \\ \omega_{ib}^b + X_e([4\ 5\ 6]) \end{bmatrix} + w_i \tag{31}$$

The IMU measurement covariance matrix is obtained from the simulated error characteristics presented in the next section. The observation model for the GNSS observables is given by:

$$Z_{GNSS} = \begin{bmatrix} \rho_r^s + X_{clk}(1) \\ -(\frac{f_i}{c}([v_{es}^e - v_{er}^e]^T e_r^s + X_{clk}(2)) \end{bmatrix} + w_g \tag{32}$$

In (32), it is assumed that the raw observables have been corrected for any ionospheric and tropospheric delay effects as well as satellite clock effects, including relativistic effects. The different models used in simulating and correcting these effects will be explained in the next section. $v_{es}^e$ and $v_{er}^e$ represent the satellite and receiver velocity vectors in the ECEF frame, respectively. The geometric range ($\rho_r^s$) and line of sight vector ($e_r^s$) from the receiver to the satellite are given by:

$$\rho_r^s = \left|\left|r_{es}^e - r_{er}^e\right|\right| + \frac{\omega_{ie}}{c}(y_{es}^e\, x_{er} - x_{es}^e\, y_{er}) \tag{33}$$

$$e_r^s = \frac{r_{es}^e - r_{er}^e}{||r_{es}^e - r_{er}^e||} \tag{34}$$

In (33) $r_{es}^e$ is the ECEF frame position vector for the satellite ($s$), $r_{er}^e$ is the receiver's ECEF frame position vector and $c$ is the speed of light in free space. The approximation in (33) accounts for the Sagnac effect as a result of using the ECEF frame. The NED to ECEF frame transformation matrix ($R_n^e$) is given by:

$$R_n^e = \begin{bmatrix} -\cos(\lambda)\sin(\mu) & -\sin(\lambda) & -\cos(\lambda)\cos(\mu) \\ -\sin(\lambda)\sin(\mu) & \cos(\lambda) & -\sin(\lambda)\cos(\mu) \\ \cos(\mu) & 0 & -\sin(\mu) \end{bmatrix} \tag{35}$$

In the filter, the variance for a given pseudorange measurement from a satellite is given by:

$$\sigma_s^2 = R_\sigma\left(a_\sigma^2 + \frac{b_\sigma^2}{\sin(E^s)}\right) + \sigma_{cbias}^2 + \sigma_{sclock}^2 + \sigma_{iono}^2 + \sigma_{tropo}^2 \tag{36}$$

In (36), $a_\sigma$ and $b_\sigma$ are set to 0.003 m. $R_\sigma$ is the code to carrier error ratio and is set to 300. $E^s$ is the satellite elevation, $\sigma_{cbias}$ is the standard deviation of the code bias error set to 0.2 m. The standard deviation of the broadcast clock error, $\sigma_{sclock}$, is set to 1.0 m. The standard deviation of the residual ionospheric delay, $\sigma_{iono}$, is set to half of the computed value for the total delay. The standard deviation of the residual tropospheric delay is given by: $\sigma_{tropo} = 0.2/(\sin(E^s) + 0.1)$. The standard deviation for the Doppler frequency measurements is set to 0.75 Hz.

## III. SIMULATION SETUP

### A. TRAJECTORY

This section presents the simulation setup, including some details of the GNSS simulator used to derive the raw observables. It should be noted that, in the simulation, guidance and control is independent of the developed architecture and utilises error-free sensors to generate the reference trajectory. 100 Monte Carlo runs are used to investigate the performance of the proposed architecture, and the interested reader is directed to [11] on the justification of the number of simulations chosen.

Fig. 3 shows the trajectory derived using error-free sensors. The flight lasted 340 seconds, and it was assumed that it took place in GPS week 2042, on the 61st day of the year (DOY) and 568800 seconds into the GPS week.

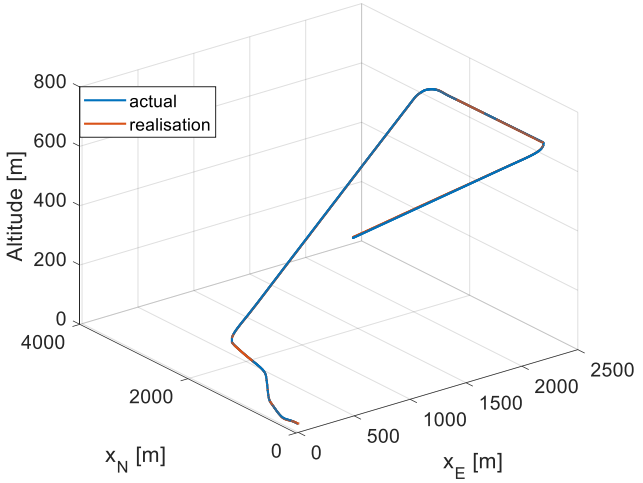


**FIGURE 3. 3D flight profile and the realisation.**

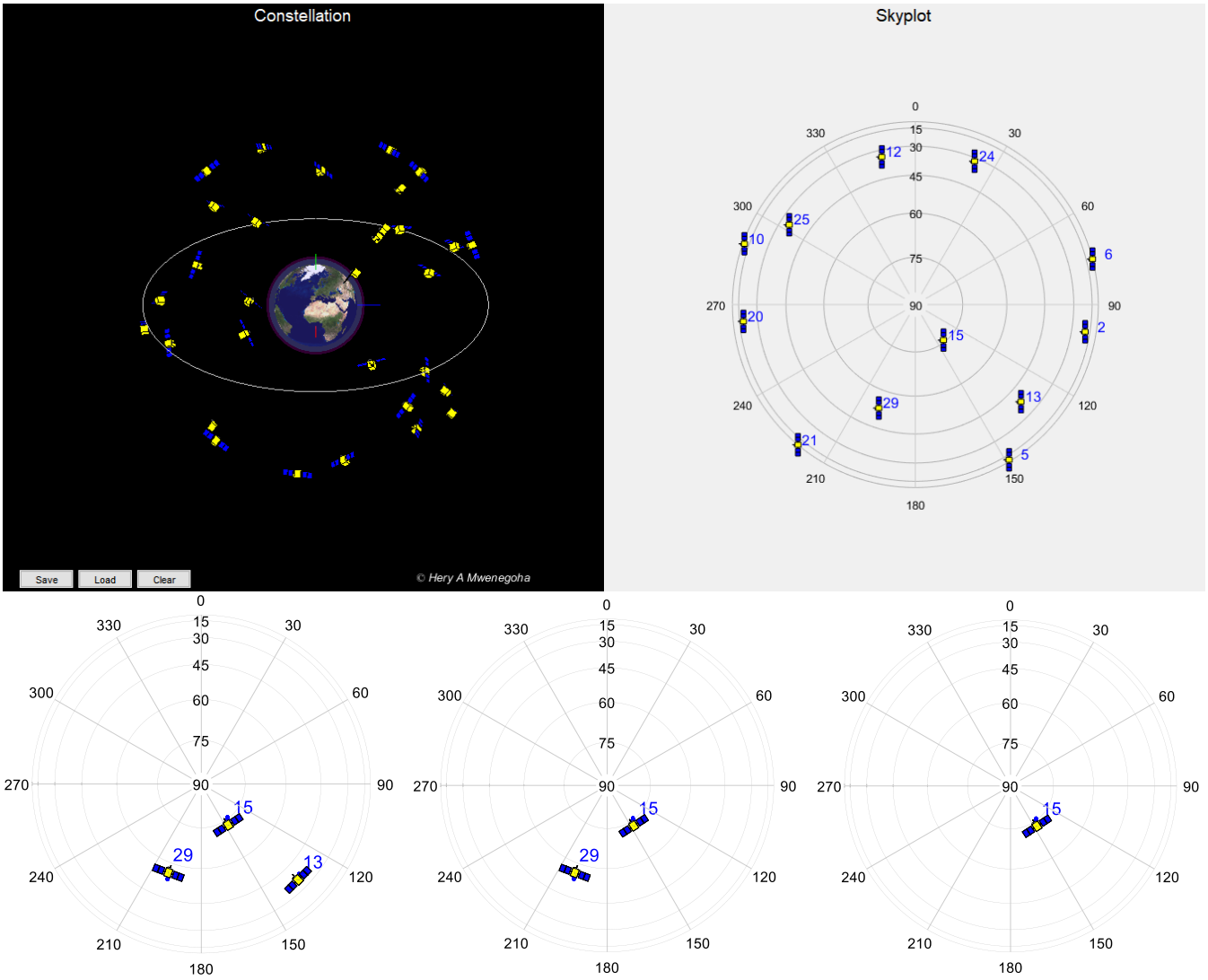


**FIGURE 4. GNSS measurement simulator with skyplots showing satellite visibility before and during a GNSS outage.**

### *B. GNSS-SIMULATOR*

Fig. 4 shows a GNSS measurement simulator that was developed to simulate raw observables output by a GNSS receiver. The user trajectory is input to the simulator to generate a series of raw observables. Hourly ephemeris products archived by the Crustal Dynamics Data Information System (CDDIS) are used to derive satellite orbits and the user ephemeris structure object [20].

Fig. 4 also shows the satellites available during an induced GNSS outage. The outage is induced 200 seconds into the flight and remains for the duration of the flight. In the TCVDM architecture, a mask angle of 15° is used to preclude low elevation satellite observations and as a result, measurements from only eight satellites were used in the first 200 seconds (during the GNSS availability period).

The pseudorange ($P_r^s$) and Doppler frequency ($D_r^s$) as modelled in the simulator are given by:

$$P_r^s = \rho_r^s + c\big(dt_r(t_r) - dT_s(T_s)\big) + I_r^s + T_r^s + M_P + \epsilon(\rho) \tag{37}$$

$$D_r^s = -\frac{f_i}{c}\left\{\begin{array}{c}[v^s(T_s) - v_r(t_r)]^T e_r^s \; + \\ c\left(\frac{\partial t_r(t_r)}{\partial t} - \frac{\partial T_s(T_s)}{\partial t}\right) + \dot{I}_r^s + \dot{T}_r^s + \dot{M}_P\end{array}\right\} + \epsilon(f_D) \tag{38}$$

where $dt_r$ and $dT_s$ are the receiver and satellite clock offsets at reception ($t_r$) and transmission time ($T_s$), respectively. $I_r^s$ and $T_r^s$ are the ionospheric and tropospheric delays, respectively, $M_P$ is the error due to multipath, $\epsilon(\rho)$ and $\epsilon(f_D)$ represent the random thermal noise and other effects. The GPS constellation, assuming the legacy L1 C/A ranging codes, is used in deriving the measurements in the simulator.

The Klobuchar model [21] is used to approximate the ionospheric delay. The parameters are perturbed with a standard deviation of 10% and then passed to the user ephemeris structure object. Further, a common residual zenith ionospheric delay is modelled as a first-order Gauss-Markov process with a standard deviation of 2 m and a time constant of 1800 s and applied to different satellites in view following appropriate mapping. The Klobuchar model is highly correlated and therefore cannot represent short term ionospheric effects very well. However, the investigation of

the impact of short term variations on navigation performance is beyond the scope of this study. Therefore, the model can be used to investigate the performance of the proposed architecture.

The European Geostationary Navigation Overlay Service (EGNOS) model [22] is used to approximate the tropospheric delay based on a set of meteorological parameters. The zenith total delay (ZTD) is computed and mapped appropriately based on the elevation of the satellite. A residual zenith delay following a first-order Gauss-Markov process with a standard deviation of 0.2 m and a time constant of 1800 seconds is applied to all satellites following appropriate mapping. The filter utilises the Saastamoinen model to correct the total delay.

In the simulator, multipath is modelled using a first-order Gauss-Markov process with an elevation-dependent standard deviation in the range of 0.5 - 1.18 m and a time constant for each satellite in the range of 3 – 40 seconds. Multipath was not estimated in the filter. The measurement variance was adjusted to reflect the uncertainty arising from multipath effects.

Further details on the clock error model and thermal noise effects, including the validation effort can be found in [23]. Other error sources such as antenna phase centre offset (PCO), phase centre variation (PCV) and inter-frequency biases are not considered.

Table II presents a summary of the modelling effort with specific settings to each model.

TABLE II.
GNSS SIMULATOR ERROR CHARACTERISTICS

| | | |
|---|---|---|
| **Ionospheric residual** | | |
| First-order Gauss-Markov ($\sigma_{GM}$) | | 2 m |
| Correlation Time ($\tau$) | | 1800 s |
| **Tropospheric residual** | | |
| First-order GM ($\sigma_{GM}$) | | 0.2 m |
| Correlation Time ($\tau$) | | 1800 s |
| **Multipath** | | |
| GM-driving noise $\sigma_{WN} = c_0 + c_1 e^{-\frac{Elev}{c_2}}$ | $c_0$ | 0.47 m |
| | $c_1$ | 0.78 m |
| | $c_2$ | 20.92° |
| Correlation Time ($\tau$) | | 3 - 40 s |
| **Thermal noise** | | |
| $\epsilon(\rho) \sim N(0, \sigma_e^2(CN0_r^s)$ $\sigma_e^2 = c_0 + c_1 . e^{\frac{CN0_r^s - c_2}{c_3}}$ | $c_0$ | 0.05 m |
| | $c_1$ | 1.05 m |
| | $c_2$ | 28.0 dB-Hz |
| | $c_3$ | 8.0 dB-Hz |
| **GNSS receiver clock** | | |
| Clock offset ($\sigma$) | | 10 km |
| Clock drift ($\sigma$) | | 20 m/s |
| Clock drift PSD | | $0.1884\ \mathrm{m/s^{\frac{3}{2}}}$ |
| Sampling Frequency | | 1 Hz |

### C. ERROR CHARACTERISTICS

Table III shows the characteristics of the IMU. The adopted model reflects a low-cost MEMS-grade IMU. In the simulator, thermal effects, g-dependent biases and cross-coupling effects are not considered. It is important to note that the exact error characteristics are not used in the filter to reflect a situation close to reality that the error characteristics cannot be truly known.

TABLE III.
IMU ERROR CHARACTERISTICS

| **Property** | **Accelerometer** | **Gyroscope** |
|---|---|---|
| Random bias ($\sigma$) | 40 mg | 1000 °/hr |
| White noise (PSD) | 1 mg/$\sqrt{\text{Hz}}$ | 252°/hr/$\sqrt{\text{Hz}}$ |
| First-order Gauss–Markov | 0.05 mg | 20 °/hr |
| Correlation Time ($\tau$) | 200 s | 200 s |
| Sampling Frequency | 100 Hz | 100 Hz |

The standard deviation of the initial uncertainty of the states is presented in Table IV. The initial error considered for the states is such that $\delta x \sim N(0, \sigma_0^2)$. It should be noted that the filter was not sensitive to minor scaling of the initial uncertainties.

TABLE IV.
INITIAL STATE UNCERTAINTY

| **State** | **Standard deviation ($\sigma$)** |
|---|---|
| Position | $[2, 2, 3]$ m |
| Velocity | $[1, 0.5, 0.5]$ m/s |
| Attitude | $[3.5°, 3.5°, 5°]$ |
| Rotation rates | 1.5 °/s |
| Propeller speed | 15 rad/s |
| Model parameters | 10% |
| Clock offset | 10^4 m |
| Clock drift | 10 m/s |

The standard deviation of the process noise considered in the simulation is presented in Table V.

TABLE V.
PROCESS NOISE FOR THE STATES

| **State** | **Standard deviation ($\sigma$)** |
|---|---|
| $x(1{:}13)$ | $10^{-4}$ |
| $X_e([1\ 2\ 3])$ | $2 \times 10^{-5}$ |
| $X_e([4\ 5\ 6])$ | $2 \times 10^{-6}$ |
| $X_w$ | 0.005 |
| $X_p$ | 0.015% of True Values |
| $X_{clk}$ | [0.01, 0.02] |

The process noise covariance ($Q_k$) is given by:

$$Q_k = \begin{bmatrix} Q_{x(1:13)} & 0 & 0 & 0 & 0 \\ 0 & Q_{X_e} & 0 & 0 & 0 \\ 0 & 0 & Q_{X_w} & 0 & 0 \\ 0 & 0 & 0 & Q_{X_p} & 0 \\ 0 & 0 & 0 & 0 & Q_{X_{clk}} \end{bmatrix} \quad (39)$$

## IV. SIMULATION RESULTS

Results are presented with three and two satellites visible during the outage as an earlier study [23] indicated insignificant performance enhancement with one satellite

available during the GNSS outage.

Fig. 5 shows the root mean squared (RMS) of accelerometer and gyroscope bias estimation errors with two satellites visible during the outage for all 100 runs. About 90% of the initial errors were resolved well within the first 40 seconds of GNSS availability and the estimation continued to improve even during the GNSS outage. Further, the filter's $1\sigma$ prediction was consistent with the empirical root mean squared error due to the correctness of the filter setup. The continued estimation of the biases even during the GNSS outage is attributed to the improved observability due to the use of the VDM.

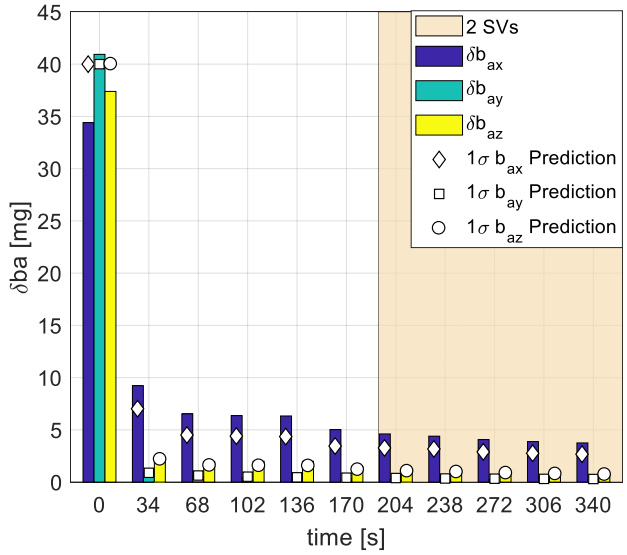


(a) Accelerometer bias.

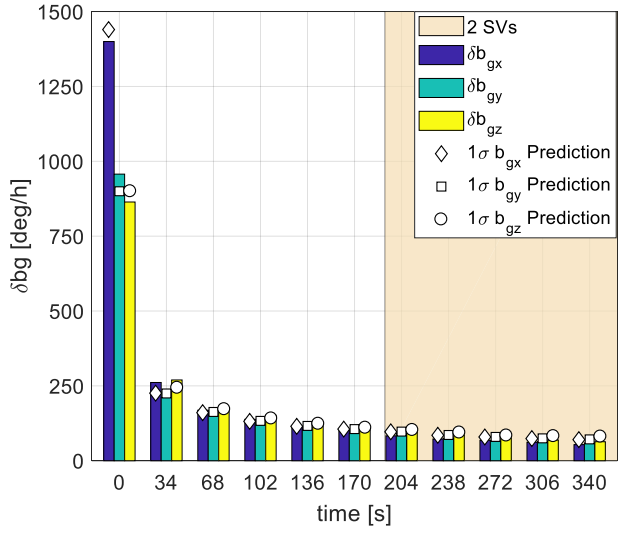


(b) Gyroscope bias.

**FIGURE 5. Accelerometer (a) and Gyroscope (b) bias estimation.**

Fig. 6 shows the attitude estimation results of the TCVDM architecture compared to an INS-based tightly coupled approach. Firstly, most of the attitude errors were resolved well within 100 seconds of GNSS availability. With three satellites visible during the outage, the attitude estimation errors of the TCVDM architecture seemed to be slightly higher than those of the INS-based scheme. The final RMS of estimation errors for roll, pitch and yaw with three satellites visible were 0.12°, 0.26°, and 0.74°, respectively, while for the INS-based scheme the errors were 0.06°, 0.09°, and 0.23° respectively. However, with two satellites visible, the final RMS of roll error for the VDM-based scheme increased by 25% to 0.15° while for the INS-based it increased by a factor of 6 to 0.36°.

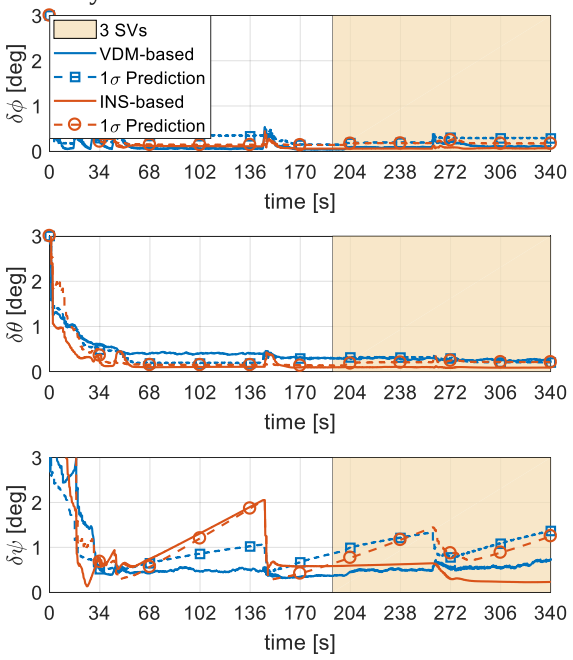


(a) Orientation errors with 3 satellites.

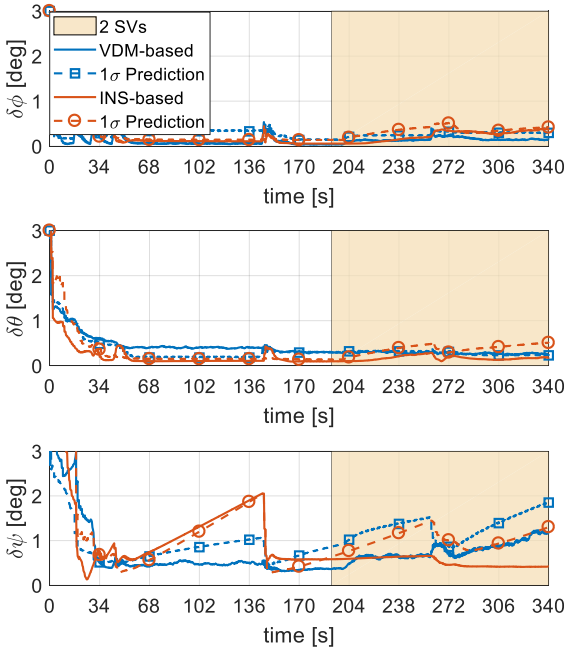


(b) Orientation errors with 2 satellites.

**FIGURE 6. Attitude estimation results for the TCVDM and INS-based architecture with three (a) and two (b) satellites visible during the GNSS outage.**

On the other hand, the final RMS of pitch error for the VDM-based scheme stayed the same while it increased by a factor of 2 for the INS-based scheme. The final RMS of yaw error

increased by 57% and 78% for the VDM- and INS-based schemes, respectively. As the number of satellites decreased, attitude errors grew rapidly for the INS-based scheme whilst the growth was gradual for the VDM-based scheme and this was especially true for roll and pitch. This gradual growth in attitude errors is due to the extra mitigation provided by the dynamic model of the aircraft.

Fig. 7 shows the RMS of velocity errors.

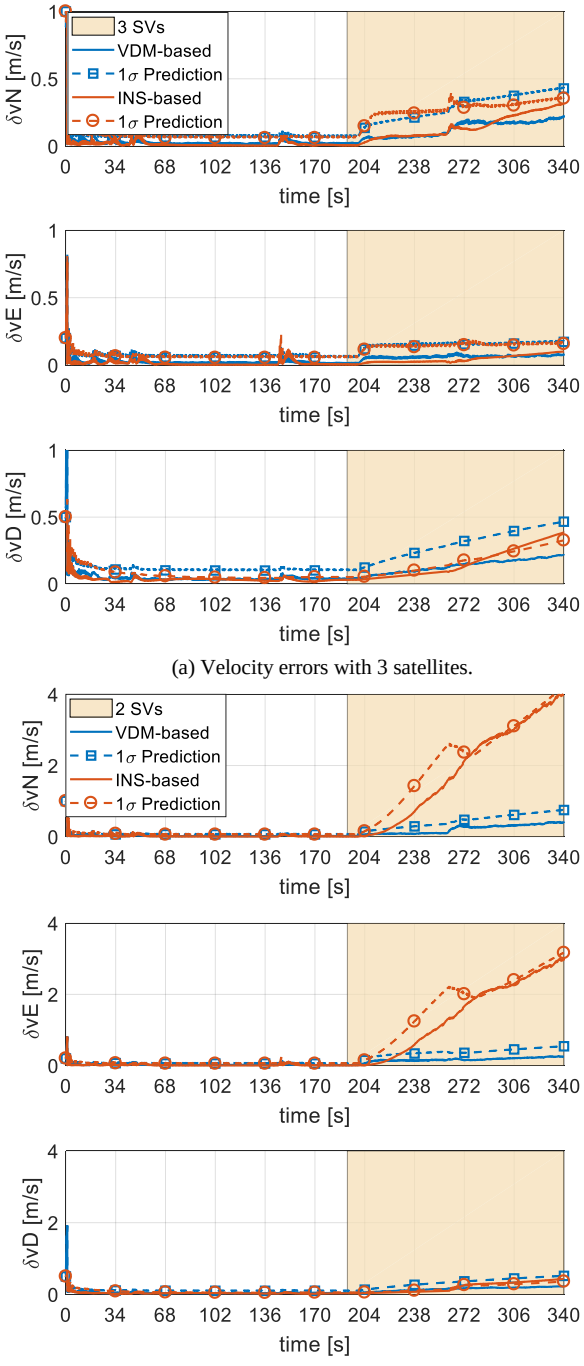


(a) Velocity errors with 3 satellites.




(b) Velocity errors with 2 satellites.

**FIGURE 7. RMS of velocity estimation errors with three (a) and two (b) satellites visible during the GNSS outage.**

The velocity errors for INS-based scheme increased rapidly as the number of satellites visible decreased during the GNSS outage. However, the VDM-based scheme showed very gradual growth in velocity errors reaching only 0.4m/s, 0.24m/s and 0.22 m/s in north, east and down directions with two satellites visible during 140 seconds of the outage. This was an order of magnitude better in the north and east channels as opposed to the INS-based scheme.

Fig. 8 shows the position error of the VDM-based architecture compared to an INS-based architecture. Generally, the position error for the VDM-based scheme with three and two satellites in view was found to be better as opposed to INS-based navigation thanks to the mitigation provided by the dynamic model that improved the observability of position errors during the outage. The position error at the end of the flight for the INS-based scheme was an order of magnitude larger than the VDM-

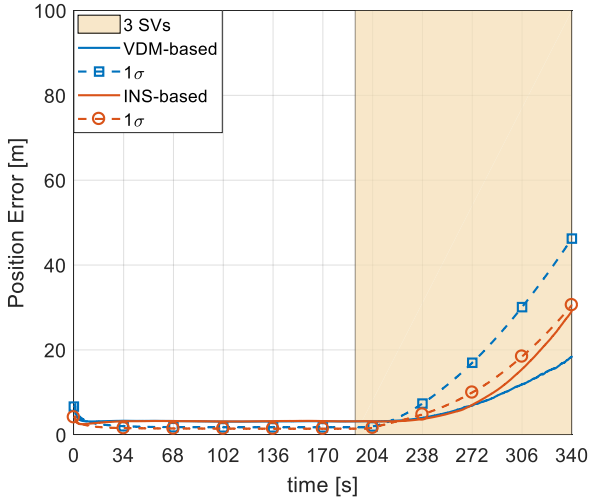


(a) Position error with 3 satellites.

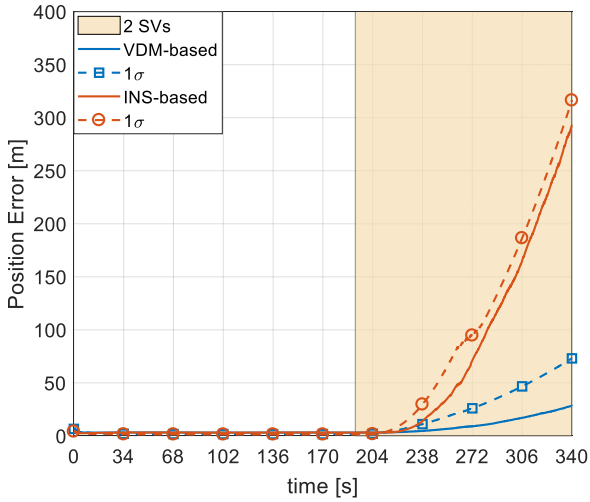


(b) Position error with 2 satellites.

**FIGURE 8. Position error with three (a) and two (b) satellites visible.**

based scheme with two satellites visible during the GNSS outage. It is also important to mention that the filter seemed slightly optimistic in height estimation leading to an overall optimistic nature in the 3D position error. This is attributed mostly to the residual range biases that are not directly estim-

mated within the filter making the overall error appear slightly larger.

Fig. 9 shows the RMS of errors in estimation of wind speed and VDM parameters. The estimation error of the VDM parameters seemed not to be affected by the decrease in the number of satellites visible during the GNSS outage thanks to the available IMU measurements and remaining raw GNSS observables. The error in estimation of wind speed seemed to increase with decreasing number of satellites during the outage but the difference with three and two satellites is less than 10%. Turning seemed to slightly improve the observability of wind errors as can be seen in Fig. 9 around 260 seconds. However, a straight and level flight following a turn seemed to reduce the filter's confidence in wind estimation as can be seen from 272 seconds to the end of the flight. Only 40% of the initial VDM parameter uncertainty was resolved by the filter mainly due to correlation within groups of the parameters but, for an initial uncertainty of 10%, the performance enhancement was sufficient to enable navigation during the GNSS outage.

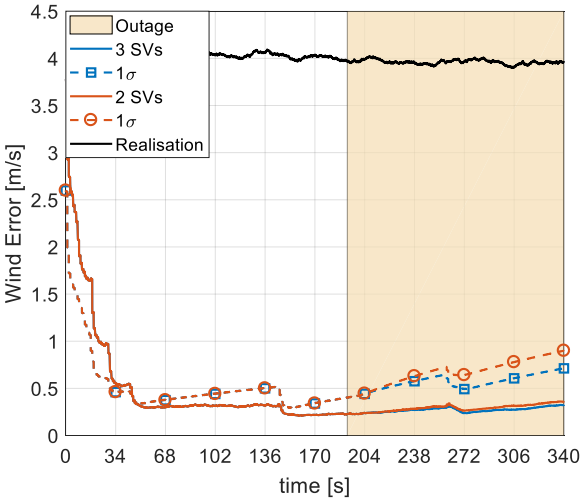


(a) Wind error.

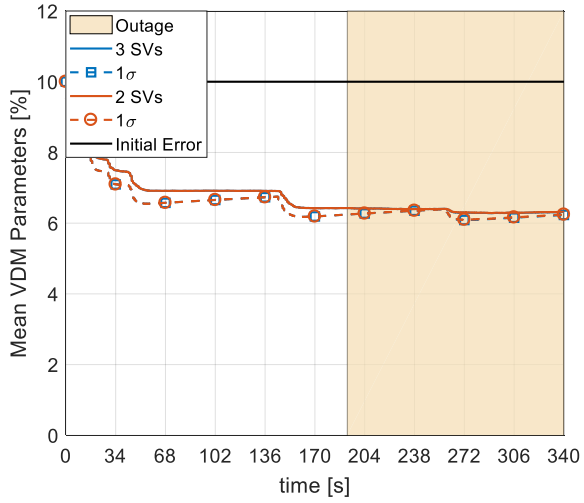


(b) VDM parameters.

**FIGURE 9. Wind estimation errors (a) and mean VDM parameters error (b) with three satellites visible during the GNSS outage.**

The RMS of the receiver clock bias and drift errors are presented in Fig. 10 with three and two satellites visible during the GNSS outage lasting 140 seconds. The clock bias error for TCVDM architecture showed gradual growth during the GNSS outage reaching only 17 meters with two satellites in view. This was only 5% higher than with three satellites in view. With two satellites in view the VDM-based scheme was better than the INS-based scheme by a factor of five in the estimation of the clock bias error. The final clock drift error for the VDM-based scheme was 6 times better than drift estimated by the INS-based scheme with two satellites visible during the outage. The improved performance of the navigation states of the VDM-based scheme helped reduce rapid growth in the clock bias and drift errors experienced by the INS-based scheme during the outage. The $1\sigma$ prediction of the clock bias for both, the VDM- and INS-based schemes, seemed optimistic during GNSS availability due to other range biases that were not estimated within the filter which led to increased error in the clock bias and position states.

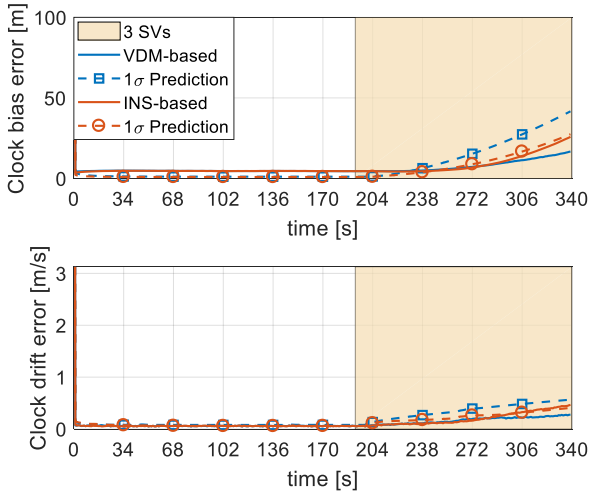


(a) Receiver clock errors estimation with 3 satellites.

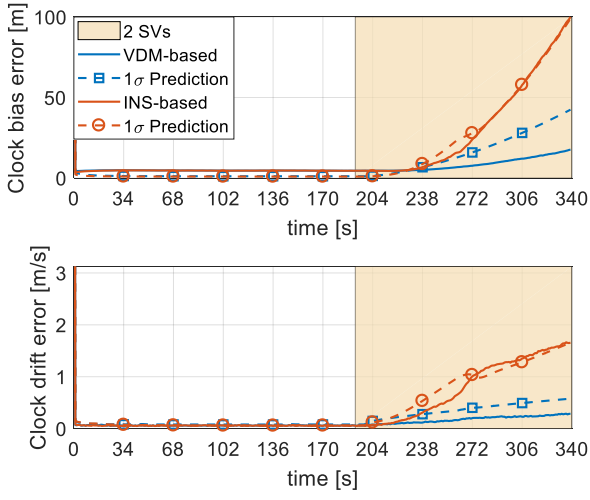


(b) Receiver clock errors estimation with 2 satellites.

**FIGURE 10. Clock bias and drift with three (a) and two (b) satellites visible during the GNSS outage.**

Fig. 11 shows a realisation of the correlation plots before the outage, 100 seconds into the flight and at the end of the outage with two satellites visible. During GNSS availability, the clock bias showed significant correlation with the down component of the position vector; this helps explain the optimistic nature of the spherical position error during GNSS availability. During an outage, the clock bias and drift terms showed significant correlation with the down components of position, velocity and wind, which helped mitigate rapid error growth during this period. VDM parameters showed significant correlation within groups and some correlation with other navigation states. The correlation with other navigation states is essential for the overall VDM parameter observability and is trajectory dependent but even for a very modest flight profile, 40% of the initial uncertainty can be resolved.

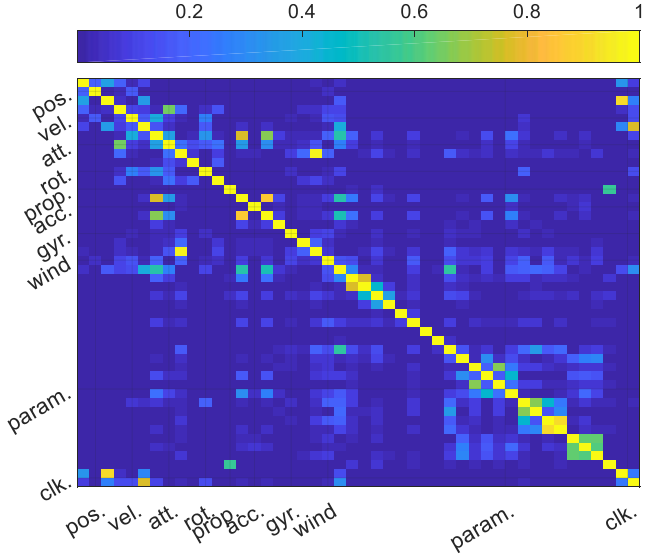


(a) Before the GNSS outage.

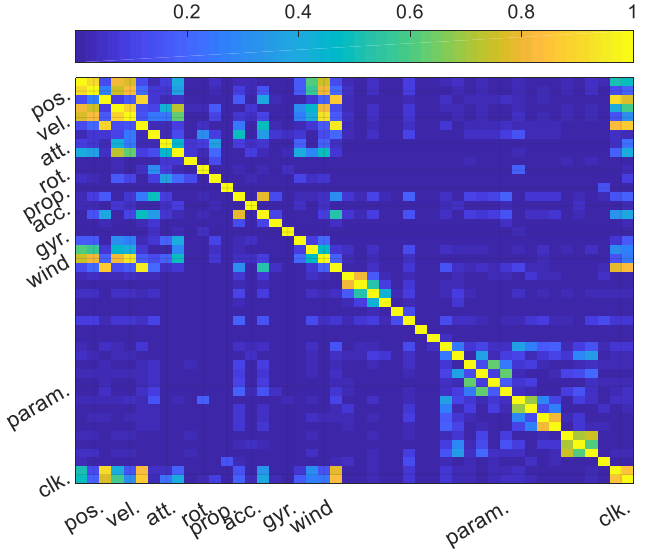


(b) After the GNSS outage.

**FIGURE 11. Correlation before (a) and after (b) the GNSS outage. (a) is 100 seconds into the flight and (b) is the correlation at the end of the flight with two satellites visible.**

## V. EXPERIMENTAL VALIDATION

### A. ON-BOARD SETUP

We modified an off-the-shelf platform and fitted it with a custom flight control system (FCS) integrated with a MEMS-grade IMU, barometer, magnetometer and a data logger. The equipment consisted of:

- NXP 9-DOF IMU – Sampled at 100Hz, this unit was used to measure the specific force components and rotation rates used for guidance and navigation.
- BMP388 – Sampled at 25Hz, this barometric pressure sensor was used for vertical channel damping.
- NEO-M8T – with an output rate of 4Hz, three GNSS receivers were used on the platform with data from the modules used in post-processing to validate the proposed architecture.
- ATmega2560 – this embedded platform was used for guidance, navigation, and control of the aircraft. The unit combines 256KB ISP flash memory, 8KB SRAM and 4KB EEPROM. The unit achieves a throughput of 16MIPS at 16MHz.
- Openlog – based on an ATmega328 running at 16MHz, this board was used for logging data from the IMU, BMP388, GNSS receivers and control inputs at 20Hz.
- RIOT V2 – the aircraft used in our investigation.

The total equipment cost was around £1200.

### B. FLIGHT CONTROL SYSTEM AND GROUND CONTROL STATION

Fig. 12 shows the custom FCS and ground control system (GCS) used during the tests.

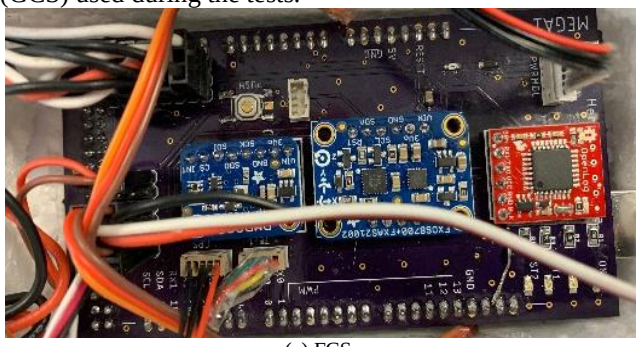

(a) FCS.

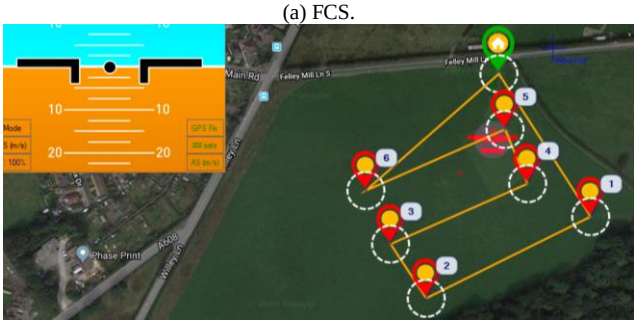


(b) GCS.

**FIGURE 12. Custom flight control system and ground control station.**

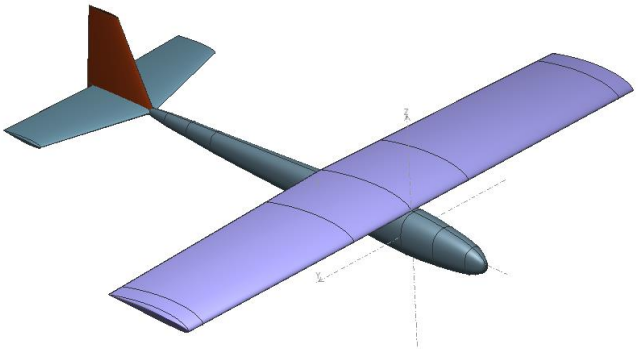

(a) XFLR5 geometry.

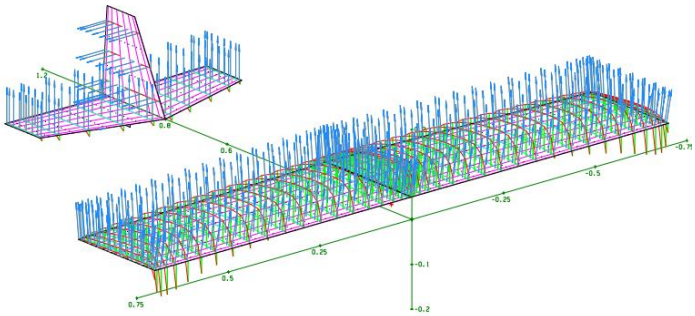

(b) AVL input.

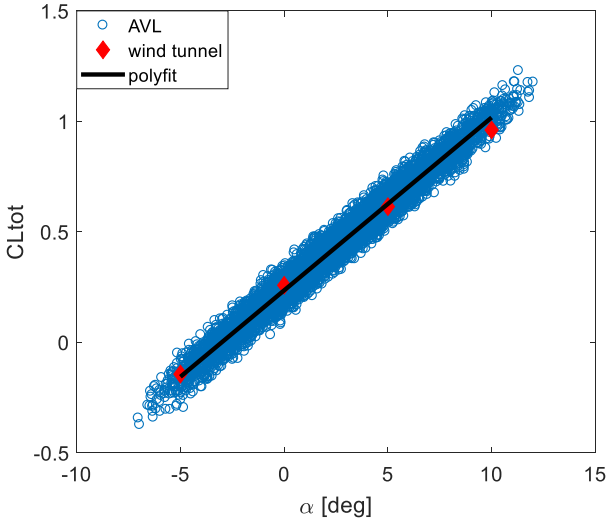


(c) AVL solution : Lift coefficient.

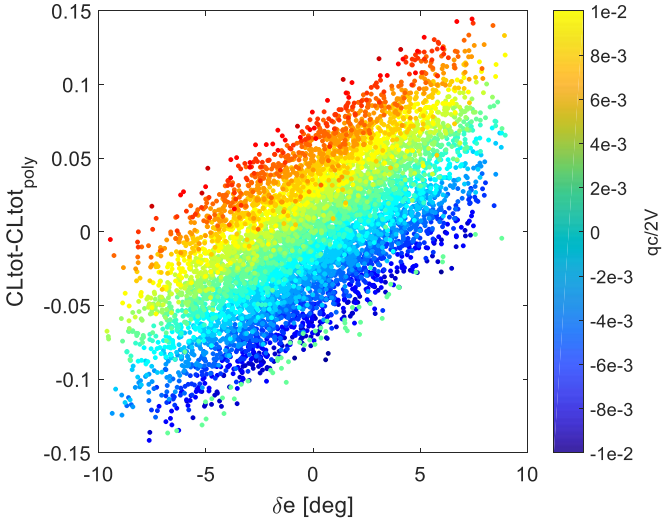


(d) Polynomial reduction.

**FIGURE 13. Aircraft characterisation workflow. The XFLR5 geometry (a) is exported to AVL (b) without the fuselage for aerodynamic analysis. Eight input variables are used in the potential flow solver to generate solutions (c). In (c), the total lift coefficient is plotted against the angle of attack. Reduced polynomial fitting (d) is used to determine appropriate monomials. In (d), the reduced lift coefficient is plotted against aileron deflection.**

The FCS handled control inputs from the pilot in manual mode and carried out a pre-programmed mission in autopilot mode. The GCS was used to program the mission profile, change aircraft settings whenever necessary and log incoming telemetry from the aircraft.

### C. AIRCRAFT CHARACTERISATION

The geometry definition is used to estimate the aerodynamic coefficients of the aircraft. This method is simple, fast, and ideal for low-cost applications. The aerodynamic parameters are estimated using an open-source potential flow solver, Athena Vortex Lattice (AVL), which provides values that are within 20% of the actual parameters [24]. The geometry is defined using a freely available aerodynamic analysis tool, XLFR5 and then after exported to AVL. Results from a Monte Carlo simulation study with eight input variables $(\alpha, \beta, \bar{\omega}_x, \bar{\omega}_y, \bar{\omega}_z, \delta_\alpha, \delta_e, \delta_r)$ are used to estimate the aerodynamic coefficients. Fig. 13 shows the workflow used in the estimation of the coefficients, including the polynomial fit from selected monomials.

Fig. 14 shows the AVL drag coefficient results following polynomial reduction and compared to available wind tunnel results. There is a noticeable offset between the reduced AVL solution and wind tunnel results attributed to the missing drag contributions in the potential flow solution. The available wind tunnel results are not used in the assessment of the experimental results obtained from our investigation due to some limitations in wind tunnel testing. For instance, the wind tunnel results were obtained on a scaled model in a clean configuration (e.g. no landing gear). They, therefore, did not truly represent the aerodynamic characteristics of the current configuration.

For the interested reader, a detailed discussion of Reynolds scaling effects and other considerations for both the wind tunnel setup and XFLR5 can be found in [25].

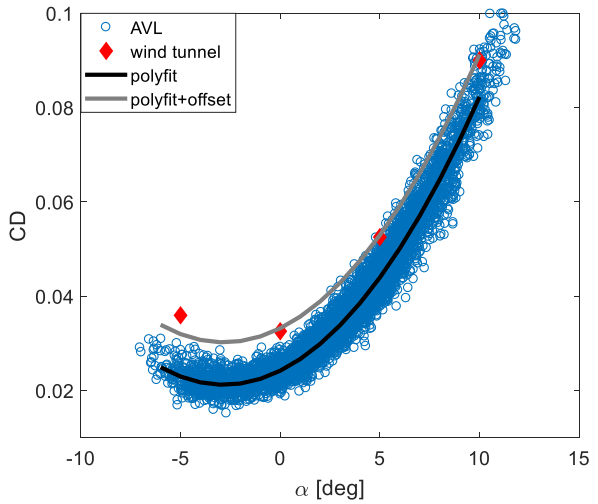


**FIGURE 14. AVL Drag coefficient with angle of attack.**

Determination of the static thrust coefficient is relatively straight forward, both simulated and experimental results [26] show good agreement to within 3% based on the evaluation of an Advanced Precision Composites (APC) 11x8 electric propeller as can be seen in Fig. 15.

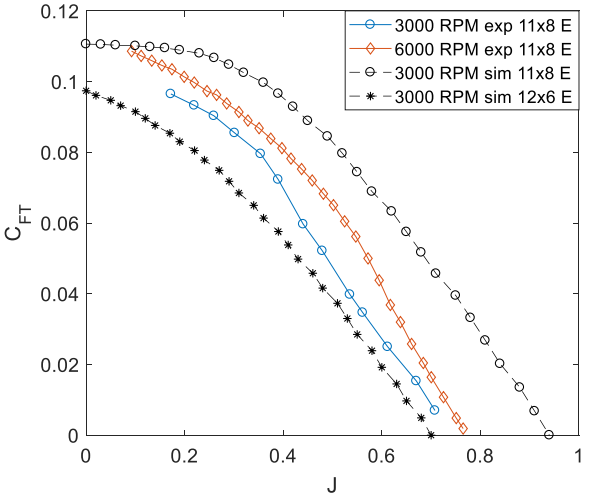


**FIGURE 15. APC 11x8 Electric propeller wind tunnel results compared to the simulated performance data available from the manufacturer** [27].

Experimental results show that the first- and second-order thrust terms show variations, especially close to the maximum efficiency region. This presents a direct challenge in our formulation because we have assumed that there is no variation in higher-order terms. Further, based on the evaluation of an APC 11x8E propeller, the error in the higher-order terms in the simulated data is found to be more than 25% when compared to the experimental results. However, the proposed architecture can refine the parameters in flight and therefore, the data provided by the manufacturer is used for the initial parameters and the uncertainties set accordingly.

Details of the aircraft geometry and mass properties are given in Table VI. It should be noted that the moment of inertia terms are also obtained from XFLR5 following the geometry definition and mass input. These terms are found to be within 7% of reference values available from full-scale oscillation tests. The aircraft characterisation process using a combination of AVL and XFLR5 provides reasonable initial estimates that can be supplemented with wind tunnel data and full-scale oscillation tests if available. A complete parameter estimation routine using onboard sensors is an attractive alternative solution to the one presented but is beyond the scope of this paper.

TABLE VI.
AIRCRAFT MASS PROPERTIES

| Property | Value |
|---|---|
| $m$ | 2.168 kg |
| $S$ | 0.36 $m^2$ |
| $b$ | 1.4 m |
| $\bar{c}$ | 0.257 m |
| $D$ | 0.3048 m |
| $I_{xx}$ | 0.12 $kgm^2$ |
| $I_{yy}$ | 0.13 $kgm^2$ |
| $I_{zz}$ | 0.24 $kgm^2$ |

Table VII shows the thrust and aerodynamic derivatives used in the validation.

TABLE VII.
AIRCRAFT STABILITY AND CONTROL DERIVATIVES

| Property | Value | Property | Value |
|---|---|---|---|
| $CF_{T_1}$ | 0.098 | $CM_{X_\beta}$ | -0.050 |
| $CF_{T_2}$ | -0.120 | $CM_{X_{\bar{\omega}_x}}$ | -0.400 |
| $CF_{T_3}$ | -0.480 | $CM_{X_{\bar{\omega}_z}}$ | 0.116 |
| $CF_{X_1}$ | -0.024 | $CM_{Y_1}$ | -0.007 |
| $CF_{X_\alpha}$ | -0.121 | $CM_{Y_\alpha}$ | -1.371 |
| $CF_{X_{\alpha^2}}$ | -1.225 | $CM_{Y_{\delta_e}}$ | 0.300 |
| $CF_{X_{\beta^2}}$ | -0.696 | $CM_{Y_{\bar{\omega}_y}}$ | -15.570 |
| $CF_{Z_1}$ | -0.235 | $CM_{Z_{\delta_r}}$ | 0.018 |
| $CF_{Z_\alpha}$ | -4.481 | $CM_{Z_{\bar{\omega}_z}}$ | -0.193 |
| $CF_{Y_1}$ | -0.096 | $CM_{Z_\beta}$ | 0.149 |
| $CM_{X_{\delta_\alpha}}$ | 0.055 | $\tau_n$ | 0.200 |

### *D. FLIGHT TESTS*

Flight tests were conducted on the 12th of September 2019 around 1500hrs at Hucknall Model Flying Club, Nottinghamshire, UK (53.048459 N, 1.291661 W). A LeicaGS10 unit was used as the ground reference GNSS receiver to derive a post-processed kinematic (PPK) position solution. Three ublox NEO-M8T GNSS receivers (GM, G1 and G2) were used on the aircraft to provide baseline solutions ($b_1$ and $b_2$) for precise attitude determination. Time differenced carrier phase (TDCP) measurements were used for precise velocity determination. The reference receiver setup and aircraft just before take-off are shown in Fig. 16.

The flight consisted of six main segments, take-off, climb, loiter, autopilot-mission, descent, and land. Take-off was conducted manually by the pilot followed by a climb segment and a quick transition to a loiter segment. These segments made up the first 200 seconds of the flight.


(a) Leica GS10. (b) Riot-V2.

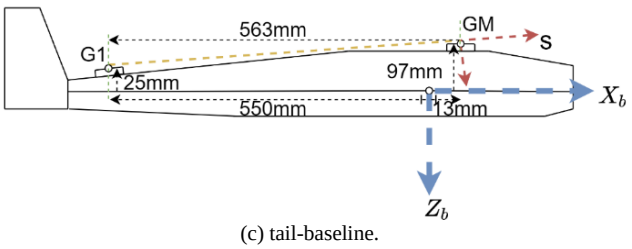


(c) tail-baseline.

**FIGURE 16.** **LeicaGS10 (a), modified riot v2 (b), and the tail-baseline vector $b_1$ between G1 and GM (c) with respect to the aircraft's centre of mass.**

In loiter mode the pilot performed a series of manoeuvres such as S-turns, deep-dives, steep climbs to excite different modes. After this segment, the autopilot was engaged and the aircraft flew a pre-programmed mission for 120 seconds. The entire flight lasted 400 seconds.

### *E. POST-PROCESSING AND VALIDATION*

IMU measurements and control inputs were logged at 20Hz on the FCS logger whilst GNSS data was logged at 4Hz on independent data loggers for each module. The data was post-processed after the flight to derive the reference solution and validate the proposed architecture. The PPK position solution, precise GNSS attitude and TDCP velocity estimates were used as measurements in a standard INS/GNSS architecture to derive the reference solution to validate the proposed architecture as can be seen in Fig. 17.

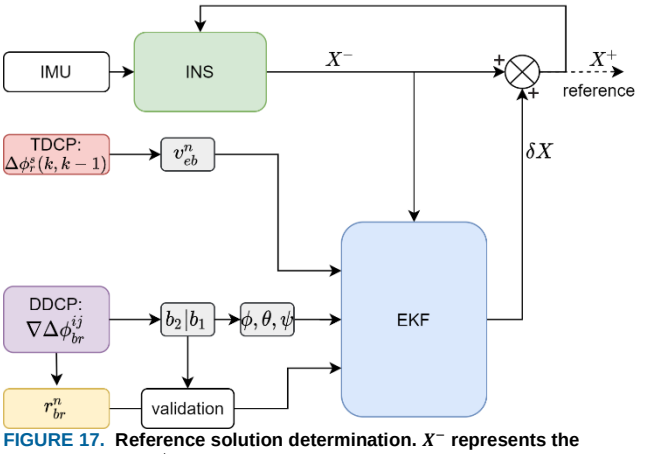


**FIGURE 17.** **Reference solution determination. $X^-$ represents the predicted state, $X^+$ represents the corrected state.**

Fig. 18 shows the number of satellites visible during the GNSS outage for two scenarios investigated. A GNSS outage was induced 246 seconds into the flight and lasted for 100 seconds. During this time the number of satellites visible was reduced by masking low elevation satellite.

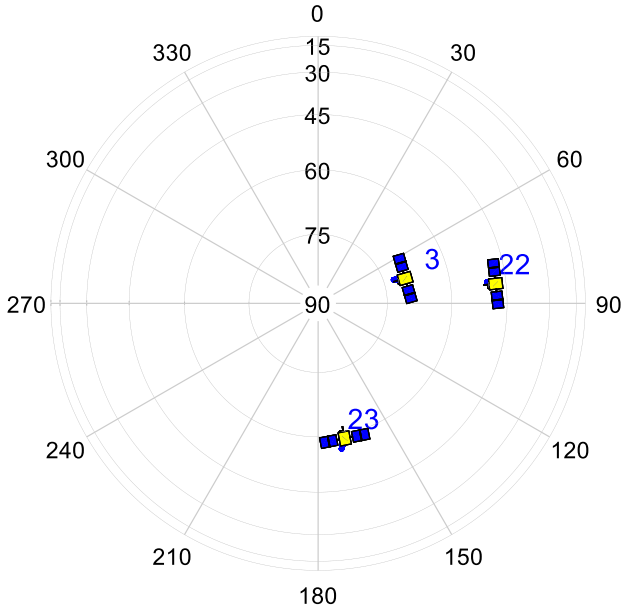


(a) Skyplot – 3 Satellites.

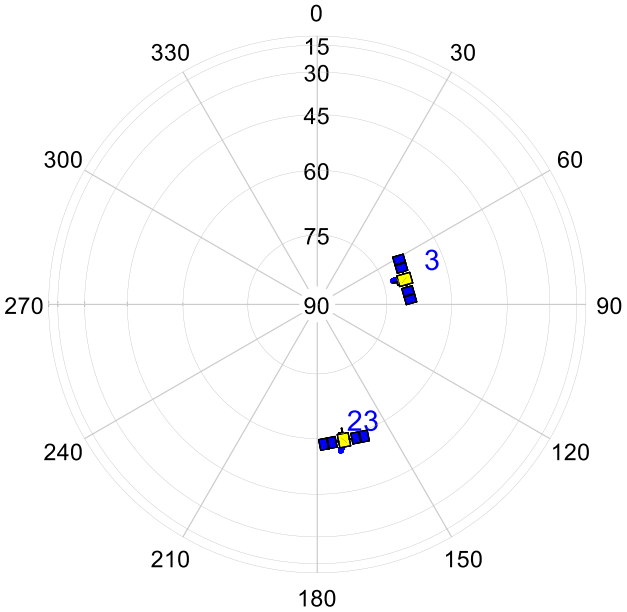


(b) Skyplot – 2 Satellites.

**FIGURE 18.** **Skyplot of the remaining satellites after inducing an outage by using an elevation masking angle of 47° for (a) and 53° for (b).**

### *F. RESULTS*

Fig. 19 shows the attitude and velocity estimates of the proposed TCVDM architecture in relation to the reference values. Generally, the TCVDM architecture followed the trend very well with a gradual decrease in performance with decreasing number of satellites in view during the GNSS outage. Table VIII shows the RMS of attitude and velocity

errors for both the proposed VDM-based scheme and a tightly coupled INS-based scheme.

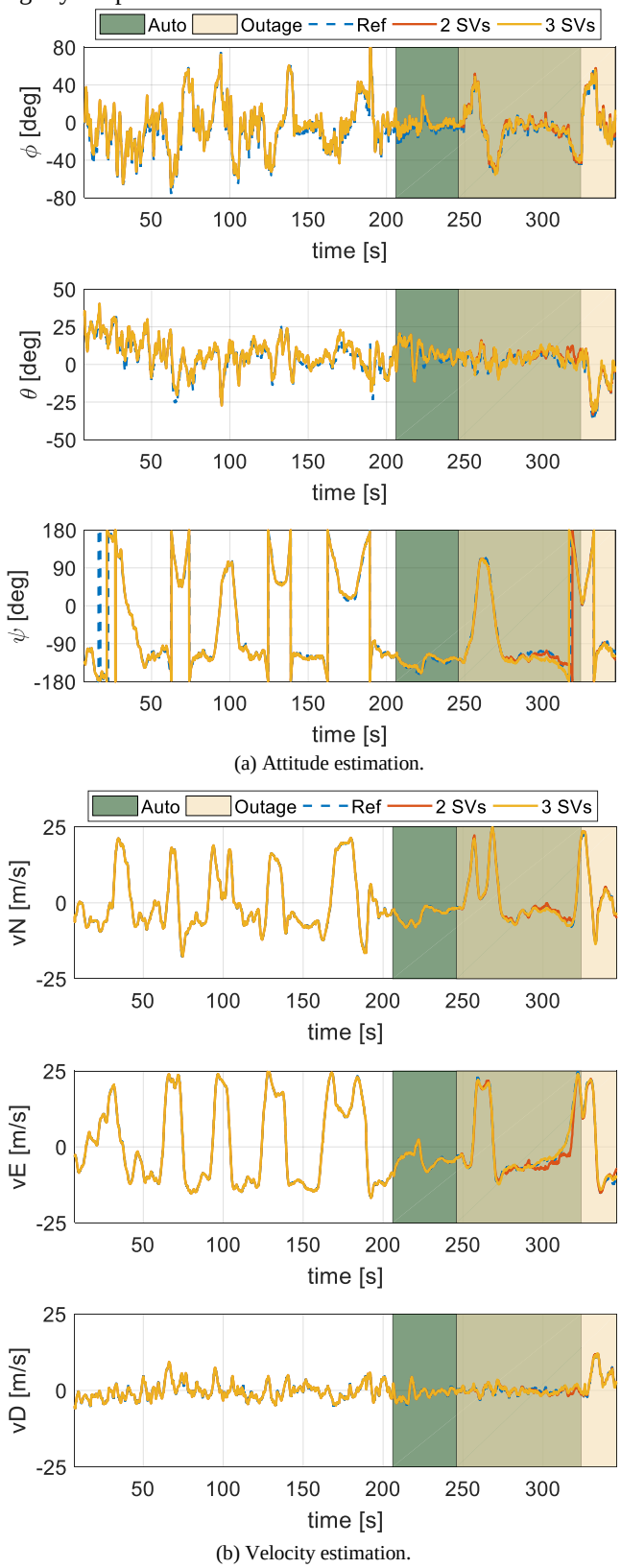


(a) Attitude estimation.

(b) Velocity estimation.

**FIGURE 19. TCVDM attitude (a) and velocity (b) estimation with two and three satellites visible during the GNSS outage.**

With two satellites visible the RMS of velocity errors for the proposed architecture showed an improvement by at least a factor of 7 in all channels as opposed to an INS-based scheme for 100 seconds of GNSS outage. Even though the trajectory used for the simulation is very different from the real flight tests, the order of errors for the north and east channels seemed to be similar.

The RMS of roll and pitch errors for the VDM-based scheme were greater by at least a factor of 2 for both scenarios as opposed to an INS-based scheme and by a factor of at least 3.5 in yaw. The VDM-based scheme showed significantly poor performance in attitude estimation as opposed to the INS-based scheme attributed mostly to the large uncertainty in the moment terms due to the limitations of the estimation routines for these terms. A rigorous parameter estimation routine could have helped improve the estimation but that was not the focus of the investigation.

TABLE VIII.
RMS ATTITUDE AND VELOCITY ERRORS

| **Attitude** | | | **Velocity** | | |
|---|---|---|---|---|---|
| SVs | INS [°] | VDM [°] | SVs | INS [m/s] | VDM [m/s] |
| | **Roll** | | | **North** | |
| 3 | 0.51 | 1.35 | 3 | 0.15 | 0.32 |
| 2 | 0.66 | 1.46 | 2 | 2.80 | 0.41 |
| | **Pitch** | | | **East** | |
| 3 | 0.51 | 1.61 | 3 | 0.22 | 0.40 |
| 2 | 0.67 | 1.61 | 2 | 8.26 | 1.11 |
| | **Yaw** | | | **Down** | |
| 3 | 0.79 | 3.26 | 3 | 0.24 | 0.39 |
| 2 | 0.92 | 3.45 | 2 | 2.49 | 0.39 |

Fig. 20 shows the spherical position error and the 2D position plots with three satellites visible during the GNSS outage. Here, the final position error of the VDM- and INS-based schemes were found to be very close, reaching only 13 m for the VDM and 19 m for the INS. However, it is important to point out that, the VDM-based scheme showed improved estimation during turns depicted by the sharp decrease in overall position error around 280 s, 310 s and 330 s while the INS-based scheme experienced gradual growth during the outage.

Fig. 21 shows the spherical position error with two satellites visible during the GNSS outage. Here, the VDM-based scheme final position error reached only 47 metres, an improvement by a factor of 43 as opposed to the INS-based scheme. The 2D position plot also shows how well the VDM-based scheme was able to track the reference position solution as opposed to the INS-based scheme even with just 2 satellites visible owing to the mitigation provided by the dynamic model.

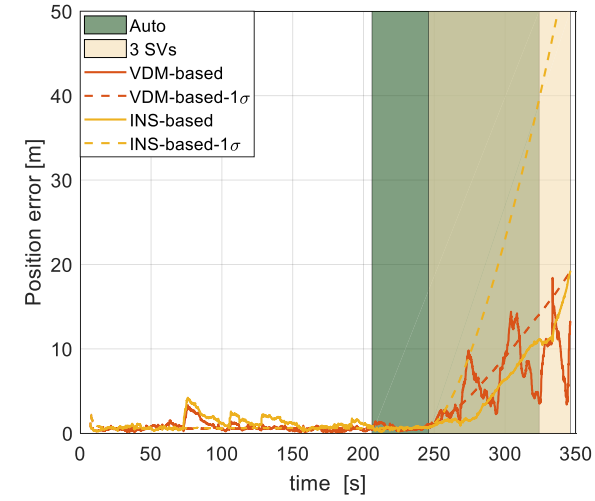


(a) 3D position.

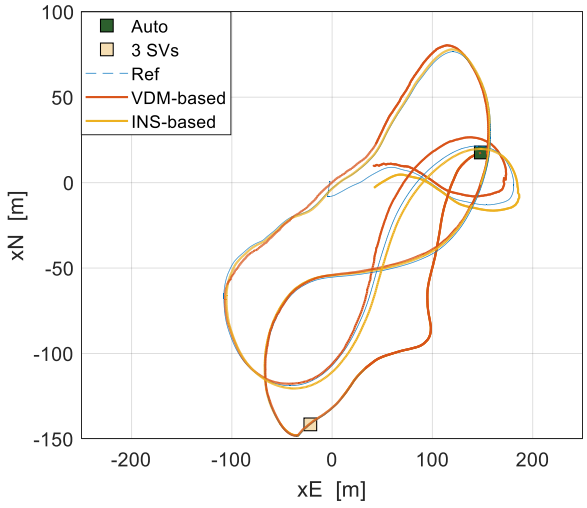


(b) 2D position.

**FIGURE 20.** **3D Position error (a) and a partial 2D position plot (b) with three satellites in view during the GNSS outage.**

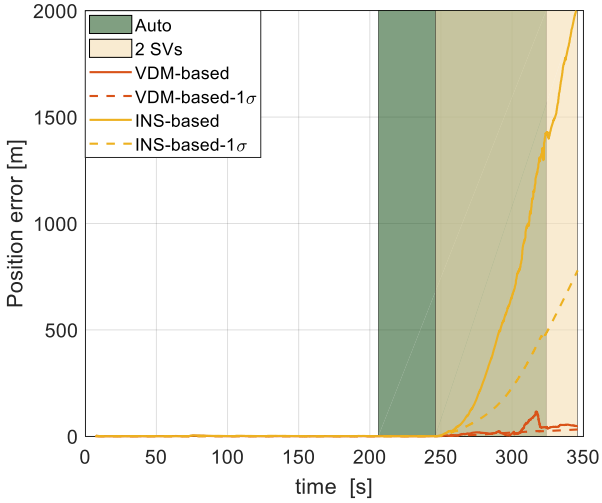


(a) 3D position.

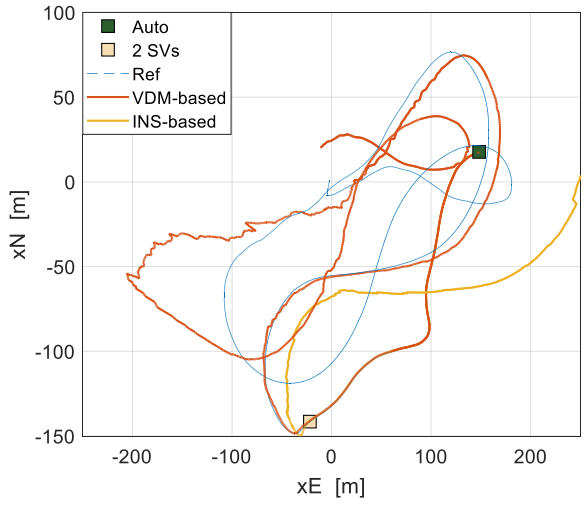


(b) 2D position.

**FIGURE 21.** **3D Position error (a) and a partial 2D position plot (b) with two satellites visible during the GNSS outage.**

## VI. CONCLUSION

A TCVDM architecture capable of utilising raw GNSS observables has been developed and tested. Results from a Monte Carlo simulation study revealed that the proposed architecture can improve position estimation by one order of magnitude with two satellites visible during an extended GNSS outage whilst offering similar attitude estimation performance compared to an INS-based scheme. Further, it was found that for a modest trajectory, the proposed architecture only captures about 40% of the initial uncertainty in the VDM parameters due to significant correlation within groups of the parameters. Other auxiliary states such as wind, IMU errors and clock errors are well estimated even with only two satellites visible.

The performance enhancements of the proposed architecture motivated the evaluation under real operational conditions. A test flight was conducted using a small modified off-the-shelf platform and the data was post-processed and the architecture evaluated. Experimental results showed significant performance enhancement in

position and velocity estimation. It was found that the RMS of estimation error for the velocity components was 7 times better across all channels with two satellites visible as opposed to an INS-based scheme. The final spherical position error was improved by at least a factor of 43 with the VDM-based scheme as opposed to an INS-based scheme. Attitude performance during the simulations revealed only marginal roll and pitch performance improvements of the TCVDM architecture using a low-cost MEMS-grade IMU as opposed to an INS-based scheme and poor performance in yaw altogether. Experimental attitude results showed even poor performance across all channels due to large uncertainties in some of the model parameters.

Generally, the position and velocity performance of the proposed architecture in an experimental setting is very promising and has shown that the scheme can be used during extended GNSS outages to provide a navigation solution. However, it is important to highlight some challenges and potential issues that, if addressed, can improve attitude performance altogether. The initial parameters used were determined from a Monte Carlo simulation study in AVL using the aircraft geometry. The resolution of some of the parameters, especially the moment derivatives, was poor, and this might have significantly contributed to the poor attitude estimation performance during the outage. Because the architecture only resolves a small amount of the initial VDM parameter uncertainty, it is important to have a reasonably good estimate of these parameters. Further, secondary effects such as actuator dynamics and delays in the actuator signal were not considered in this investigation. Actuator dynamics would have improved the fidelity of the model with an additional penalty of extra states for each control surface. A tightly coupled architecture is usually sensitive to synchronisation errors and therefore delays in the actuator signal might have contributed to the degraded performance. Such a scheme can only be used after the aircraft has taken off and before it lands, otherwise, risks biasing the states. The quality of the IMU plays an important role in attitude estimation especially when the uncertainty in the model parameters is large and therefore, effects such as large vibrations, and thermal loading could indirectly influence the performance of the architecture during an outage.

Even though the proposed architecture has only been tested in a single frequency setting, the algorithm can be used with a multifrequency GNSS receiver. Further, the algorithm could also be used in a multiconstellation setting and take advantage of improved signals with lower noise and improved multipath performance but an extensive investigation is subject to future work.

## APPENDIX

### A. ABBREVIATIONS

| | |
|---|---|
| DDCP | Double Differenced Carrier Phase |
| DOY | Day of the Year |
| ECEF | Earth-Centred Earth-Fixed |
| ECI | Earth-Centred Inertial |
| EKF | Extended Kalman Filter |
| FCS | Flight Control System |
| GNSS | Global Navigation Satellite System |
| GPS | Global Positioning System |
| IMU | Inertial Measurement Unit |
| INS | Inertial Navigation System |
| ISP | In-System Programming |
| MEMS | Micro-Electro-Mechanical System |
| MIPS | Million Instructions Per Second |
| PCO | Phase Centre Offset |
| PCV | Phase Centre Variation |
| PSD | Power Spectral Density |
| TCVDM | Tightly Coupled Vehicle Dynamic Model |
| TDCP | Time Differenced Carrier Phase |
| UAV | Unmanned Aerial Vehicle |
| VDM | Vehicle Dynamic Model |

### B. NOMENCLATURE

| | |
|---|---|
| $\alpha$ | angle of attack |
| $\beta$ | sideslip angle |
| $\delta_\alpha$ | aileron deflection |
| $\delta_e$ | elevator deflection |
| $\delta_r$ | rudder deflection |
| $\lambda$ | longitude |
| $\mu$ | latitude |
| $\rho$ | air density |
| $\sigma$ | standard deviation |
| $\tau_n$ | motor-propeller time constant |
| $\phi$ | roll angle |
| $\phi_r^s$ | carrier phase between (r) and (s) |
| $\theta$ | pitch angle |
| $\psi$ | yaw angle |
| $\omega_{en}^n$ | transport-rate |
| $\omega_{ib}^b$ | rotation rate vector in the body frame |
| $\omega_{ie}$ | Earth rotation rate |
| $\omega_x$ | roll rate |
| $\bar{\omega}_x$ | dimensionless roll rate |
| $\omega_y$ | pitch rate |
| $\bar{\omega}_y$ | dimensionless pitch rate |
| $\omega_z$ | yaw rate |
| $\bar{\omega}_z$ | dimensionless yaw rate |
| $a$ | temperature lapse rate |
| $b$ | wing span |
| $b_1$ | tail-baseline vector |
| $b_2$ | left-wing baseline vector |
| $b_{a_{\dots}}$ | accelerometer error |
| $b_{clk}$ | receiver clock offset |
| $b_{g_{\dots}}$ | gyroscope error |
| $c$ | speed of light in free space |
| $\bar{c}$ | mean aerodynamic chord |
| $CF_{T_{\dots}}$ | thrust force coefficients |
| $CF_{X_{\dots}}$ | drag force coefficients |

| | |
|---|---|
| $CF_{Y_{...}}$ | lateral force coefficients |
| $CF_{Z_{...}}$ | lift force coefficients |
| $CM_{X_{...}}$ | roll moment coefficients |
| $CM_{Y_{...}}$ | pitch moment coefficients |
| $CM_{Z_{...}}$ | yaw moment coefficients |
| $d_{clk}$ | receiver clock drift |
| $D$ | propeller diameter |
| $e_r^s$ | line of sight vector from (r) to (s) |
| $E^s$ | elevation of satellite (s) |
| $F$ | linearized dynamic matrix |
| $f_i$ | carrier frequency in the L(i) band |
| $f_{ib}^b$ | specific force in the body frame |
| $F_T$ | thrust force |
| $F_X^w$ | drag force |
| $F_Y^w$ | lateral force |
| $F_Z^w$ | lift force |
| $g$ | gravity acceleration |
| $G_{...}$ | noise shaping matrix |
| $h$ | geodetic height |
| $H$ | linearized observation matrix |
| $I^b$ | aircraft inertia matrix in body-fixed frame |
| $I_{...}$ | moment of inertia components |
| $I_r^s$ | ionospheric delay between (r) and (s) |
| $J$ | advance ratio |
| $m$ | aircraft mass |
| $M$ | vector of aircraft moments |
| $M_P$ | error due to multipath |
| $M_X^b$ | roll moment |
| $M_Y^b$ | pitch moment |
| $M_Z^b$ | yaw moment |
| $n$ | propeller speed |
| $n_c$ | commanded propeller speed |
| $p_o$ | ambient pressure at sea level |
| $\bar{q}$ | dynamic pressure |
| $q_b^n$ | quaternion rotation vector from body frame to local navigation frame |
| $q_{...}$ | quaternion component |
| $r_{br}^n$ | baseline vector between (b) and (r) |
| $r_{er}^e$ | receiver position vector in ECEF frame |
| $r_{eb}^n$ | aircraft position vector in local frame |
| $r_{es}^e$ | satellite position vector in ECEF frame |
| $R$ | gas constant for air |
| $R_b^n$ | transformation matrix from (b) to (n) |
| $R_k$ | measurement covariance |
| $R_M$ | meridian radius of curvature |
| $R_p$ | prime vertical radius of curvature |
| $R_\sigma$ | code to carrier-phase error ratio |
| $S$ | aircraft wing area |
| $t_r$ | receiver time of signal reception |
| $T_r^s$ | tropospheric delay between (r) and (s) |
| $T_s$ | satellite time of signal transmission |
| $u_{...}$ | noise vector |
| $U$ | control vector |
| $v_{er}^e$ | receiver velocity vector in ECEF frame |
| $v_{eb}^n$ | aircraft velocity vector in local frame |
| $v_{es}^e$ | satellite velocity vector in ECEF frame |
| $V$ | airspeed |
| $V^b$ | airspeed vector |
| $V_x^b$ | airspeed component along $X_b$ |
| $V_y^b$ | airspeed component along $Y_b$ |
| $V_z^b$ | airspeed component along $Z_b$ |
| $w_g$ | GNSS noise vector |
| $w_i$ | IMU noise vector |
| $w_k$ | measurement noise vector |
| $w_N$ | wind velocity component along $X_N$ |
| $w_E$ | wind velocity component along $Y_E$ |
| $w_D$ | wind velocity component along $Z_D$ |
| $W^n$ | wind velocity vector |
| $x$ | state vector |
| $X_{clk}$ | receiver clock states |
| $X_e$ | IMU error states |
| $X_n$ | navigation states |
| $X_p$ | VDM parameters |
| $X_w$ | wind velocity states |
| $Z_k$ | measurement vector |

## ACKNOWLEDGMENT

The authors would like to thank UoN colleagues for their invaluable support. We would also like to thank the Hucknall MAC administration for coordinating the flight tests.

The work is funded by the INNOVATIVE doctoral programme. The INNOVATIVE programme is partially funded by the Marie Curie Initial Training Networks (ITN) action (project number 665468) and partially by the Institute for Aerospace Technology (IAT) at the University of Nottingham.

The data used in this study were acquired as part of NASA's Earth Science Data Systems and archived and distributed by the Crustal Dynamics Data Information System (CDDIS).

## REFERENCES

[1] J. Jiménez López and M. Mulero-Pázmány, "Drones for conservation in protected areas: Present and future," *Drones*, vol. 3, no. 1, p. 24, 2019.

[2] C. A. Thiels, J. M. Aho, S. P. Zietlow, and D. H. Jenkins, "Use of unmanned aerial vehicles for medical product transport," *Air Med. J.*, vol. 34, no. 2, pp. 104–108, 2015.

[3] C. Hide, "Integration of GPS and low cost INS measurements," Ph.D thesis, Inst. of Engineering, Surveying and Space Geodesy,Uni. of Nottingham, 2003.

[4] R. Babu and J. Wang, "Ultra-tight GPS/INS/PL integration: A system concept and performance analysis," *GPS Solut.*, vol. 13, no. 1, pp. 75–82, 2009.

[5] T. K. Lau, Y. H. Liu, and K. W. Lin, "Inertial-based localization for unmanned helicopters against GNSS outage," *IEEE Trans. Aerosp. Electron. Syst.*, vol. 49, no. 3, pp. 1932–1949, 2013.

[6] A. G. Quinchia, G. Falco, E. Falletti, F. Dovis, and C. Ferrer, "A comparison between different error modeling of MEMS applied to GPS/INS integrated systems," *Sensors (Switzerland)*, vol. 13, no. 8, pp. 9549–9588, 2013.

[7] M. El-Diasty and S. Pagiatakis, "A rigorous temperature-dependent stochastic modelling and testing for MEMS-based inertial sensor errors," *Sensors*, vol. 9, no. 11, pp. 8473–8489, 2009.

[8] M. George and S. Sukkarieh, "Tightly coupled INS / GPS with bias estimation for UAV applications," in *Proc. Australiasian Conf. on Rob. and Auto. (ACRA)*, Sydney, Australia, 2005.
[9] A. Sendobry, "Control system theoretic approach to model based navigation," Ph.D thesis, Vom Fachbereich Maschinenbau,Technische Universität Darmstadt, 2014.
[10] M. Khaghani and J. Skaloud, "Autonomous vehicle dynamic model-based navigation for small UAVs," *NAVIGATION*, vol. 63, no. 3, pp. 345–358, 2016.
[11] H. Mwenegoha, T. Moore, J. Pinchin, and M. Jabbal, "Model-based autonomous navigation with moment of inertia estimation for unmanned aerial vehicles," *Sensors*, vol. 19, no. 11, p. 2467, 2019.
[12] M. Koifman and I. Y. Bar-Itzhack, "Inertial navigation system aided by aircraft dynamics," *IEEE Trans. Control Syst. Technol.*, vol. 7, no. 4, pp. 487–493, 1999.
[13] S. Zahran, A. Moussa, N. El-Sheimy, and A. B. Sesay, "Hybrid machine learning VDM for UAVs in GNSS-denied environment," *NAVIGATION*, vol. 65, no. 3, pp. 477–492, 2018
[14] W. Youn, H. S. Choi, H. Ryu, S. Kim, and M. B. Rhudy, "Model-aided state estimation of HALE UAV with synthetic AOA / SSA for analytical redundancy," vol. 20, no. 14, pp. 7929–7940, 2020.
[15] K. Mueller, P. Crocoll, and G. F. Trommer, "Model-aided navigation with wind estimation for robust quadrotor navigation," in *Proc. Int. Tech. Meeting of The Institute of Navigation*, 2016, pp. 689–696.
[16] P. Crocoll, J. Seibold, G. Scholz, and G. F. Trommer, "Model-aided navigation for a quadrotor helicopter : A novel navigation system and first experimental results," *NAVIGATION*, vol. 61, no. 4, pp. 253–271, 2014.
[17] J. F. Vasconcelos, C. Silvestre, P. Oliveira, and B. Guerreiro, "Embedded UAV model and LASER aiding techniques for inertial navigation systems," *Control Eng. Pract.*, vol. 18, no. 3, pp. 262–278, 2010.
[18] A. Gelb, J. F. Kasper, R. A. Nash, C. F. Price, and A. A. Sutherland, *Applied optimal estimation*. Cambridge, MA, London: MIT Press, 1974.
[19] R. Brown and P. Y. . Hwang, *Introduction to Random Signals and Applied Kalman Filtering*, 4th ed. Hoboken, NJ: Wiley, 2012.
[20] C. E. Noll, "The crustal dynamics data information system: A resource to support scientific analysis using space geodesy," *Adv. Sp. Res.*, vol. 45, no. 12, pp. 1421–1440, 2010.
[21] J. A. Klobuchar, "Ionospheric time-delay algorithm for single-frequency GPS users," *IEEE Trans. Aerosp. Electron. Syst.*, vol. AES-23, no. 3, pp. 325–331, 1987.
[22] N. Penna, A. Dodson, and W. Chen, "Assessment of EGNOS tropospheric correction model," *J. Navig.*, vol. 54, no. 1, pp. 37–55, 2001.
[23] H. A. Mwenegoha, T. Moore, J. Pinchin, and M. Jabbal, "Enhanced fixed wing UAV navigation in extended GNSS outages using a vehicle dynamics model and raw GNSS observables," in *Proc. 32nd Int. Tech. Meeting of the Sat. Div. of The Inst. of Navigation (ION GNSS+ 2019)*, 2019, pp. 2552–2565.
[24] A. Klöckner, "Geometry based flight dynamics modelling of unmanned Airplanes," in *AIAA Modeling and Simulation Technologies (MST) Conference*, 2013.
[25] H. A. Mwenegoha and M. Jabbal, "Investigation of passive flow control techniques to enhance the stall characteristics of a microlight aircraft," *Int. J. Flow Control*, vol. 5, no. 3, pp. 215–242, 2013.
[26] J. B. Brandt and M. S. Selig, "Propeller performance data at low Reynolds numbers," in *49th AIAA Aerospace Sciences Meeting including the New Horizons Forum and Aerospace Exposition*, 2011.
[27] APC, "APC propeller performance data," [Online]. Available: https://www.apcprop.com/. [Accessed: 31-Jul-2020].

**Hery A. Mwenegoha** has a MEng (Hons) degree in Aviation Engineering (2014) from Brunel University London. He is currently pursuing a PhD degree in engineering surveying and space geodesy at the University of Nottingham, in the United Kingdom.

From 2014 to 2017, he worked on designing Unmanned Aircraft Systems for several applications in Tanzania. His research interests include passive aerodynamic flow control for drag reduction, model-based navigation in extended GNSS outages, wavelet neural networks in aircraft parameter estimation and UAV guidance and navigation.

Hery was a recipient of the IMechE best individual project prize in 2013. In 2014 he was awarded the Royal Aeronautical Society University Prize. He is a Mandela Washington Fellow (2016).

**Professor Terry Moore** holds a BSc in Civil Engineering and a PhD in Space Geodesy both from the University of Nottingham, in the United Kingdom.

He was the Professor of Satellite Navigation at the University of Nottingham, until the end of July 2020, where he was also the Director of the Nottingham Geospatial Institute (NGI) at the University. He has many years of research experience in surveying, positioning and navigation technologies and is a consultant and adviser to European and UK government organisations and industry.

Professor Moore is a Fellow and the current President of the Royal Institute of Navigation (RIN) and also a Fellow and a Member of Council of the Institute of Navigation (ION). In 2013 he was awarded the RIN Harold Spencer-Jones Gold Medal, and in 2017 the ION Johannes Kepler Award.

**James Pinchin** is currently Assistant Professor in the Faculty of Engineering at the University of Nottingham. He received his PhD in Mechatronics Engineering from the University of Canterbury, New Zealand in 2011.

His research interests include the use of predictive models to aid systems for position and orientation determination.

Dr Pinchin is an associate fellow of the Royal Institute of Navigation (RIN).

**Mark Jabbal** has a MEng (Hons) degree (2003) and a PhD (2008) in Aerospace Engineering from the University of Manchester, UK.

He is currently Associate Professor in Aerospace Engineering at the University of Nottingham, UK. His research interests include aerodynamic flow control for drag reduction (experimental fluid mechanics; modelling and optimisation; vehicle systems integration), heat transfer for thermal management and UAV development.

Dr Jabbal is a Member of the Royal Aeronautical Society (MRAeS) and a co-opted member of the RAeS Aerodynamics Specialist Group. He is also a Fellow of the Higher Education Academy (FHEA).